TECHNICAL REPORT STANDARD PAGE

1. Title and Subtitle
Revolutionizing Civil Infrastructure with Additive Friction Stir Deposition of Stainless Steel: A Predictive Thermomechanical Modeling Approach

2. Author(s)
M Shafiqur Rahman; Pouria Nourian; Ahsanul Alam Kabhi; Sabbir Alom Shuvo

3. Performing Organization Name and Address
Department of Mechanical Engineering
Louisiana Tech University
Ruston, LA 71272

4. Sponsoring Agency Name and Address
Louisiana Department of Transportation and Development
P.O. Box 94245
Baton Rouge, LA 70804-9245

5. Report No.
FHWA/LA.26/26-3TIRE

6. Report Date
August 2026

7. Performing Organization Code
LTRC Project Number: 26-3TIRE
SIO Number: DOTLT1000592

8. Type of Report and Period Covered
Final Report
07/2025 - 06/2026

9. No. of Pages
58

10. Supplementary Notes
Conducted in Cooperation with the U.S. Department of Transportation, Federal Highway Administration

11. Distribution Statement
Unrestricted. This document is available through the National Technical Information Service, Springfield, VA 21161.

12. Key Words
Additive friction stir deposition; stainless steel; civil infrastructure; molecular dynamics; Coupled Eulerian–Lagrangian modeling; finite element analysis; thermomechanical behavior; material flow; physics-informed machine learning

13. Abstract
This project develops an integrated computational framework to study the thermomechanical behavior of stainless steel during the Additive Friction Stir Deposition (AFSD) process. This solid-state approach can reduce fusion-related defects, residual stresses, and material waste while producing dense deposits with refined microstructures. However, the application of AFSD to stainless steel remains challenging because of its high strength, work-hardening behavior, and resistance to plastic flow. Therefore, the primary process-scale component of the computational framework is a Coupled Eulerian-Lagrangian (CEL) finite element model of AISI 316L stainless steel that can capture the thermomechanical aspects of the AFSD process. The model evaluates temperature, stress, and material flow under different material and processing conditions. Molecular dynamics (MD)

simulations were also conducted to provide fundamental insight into the deformation behavior that is not directly available from continuum modeling. The MD work included tensile and shear deformation of a stainless-steel-relevant Fe–Ni–Cr alloy, with particular attention to the influence of ultrasonic vibration. The tensile MD simulations showed that vibration changed the apparent stiffness, maximum stress, kinetic energy, and internal pressure of the alloy in a nonlinear manner. The shear simulations showed that vibration reduced mean shear stress in both the elastic and flow-stress regions. Defect analysis further indicated that vibration modified dislocation initiation, rearrangement, and annihilation. The CEL model predicted thermal and mechanical responses during stainless-steel deposition and showed good agreement with published experimental peak-temperature data. The model also demonstrated that constitutive parameters, tool rotational speed, traverse speed, and material deposition rate strongly influence predicted temperature, stress, and material flow. These results provide the foundation for future physics-informed machine learning, extended FE modeling, experimental validation, and process optimization for stainless-steel AFSD. Because sufficiently large and consistent stainless-steel AFSD process–response datasets were unavailable, the physics-informed machine learning methodology was developed and validated using laser powder bed fusion data for Ti-6Al-4V. The interaction-based conditional variational autoencoder achieved R^2 values of 0.955 for the full dataset and 0.870 for an 80/20 train–test split, outperformed conventional regression and neural-network models, and demonstrated transferable forward and inverse prediction capabilities that can be retrained using future AFSD datasets without modifying the model architecture.

Project Review Committee

Each research project will have an advisory committee appointed by the LTRC Director. The Project Review Committee is responsible for assisting the LTRC Administrator or Manager in the development of acceptable research problem statements, requests for proposals, review of research proposals, oversight of approved research projects, and implementation of findings.

LTRC appreciates the dedication of the following Project Review Committee Members in guiding this research study to fruition.

LTRC Administrator/Manager

Vijaya Gopu, Ph.D., P.E.

Directorate Implementation Sponsor

Brian Owens, P.E.

DOTD Chief Engineer

Revolutionizing Civil Infrastructure with Additive Friction Stir Deposition of Stainless Steel: A Predictive Thermomechanical Modeling Approach

By
M Shafiqur Rahman
Pouria Nourian
Ahsanul Alam Kabhi
Sabbir Alom Shuvo

Department of Mechanical Engineering
Louisiana Tech University
Ruston, LA

LTRC Project No. 26-3TIRE
SIO No. DOTLT1000592

conducted for
Louisiana Department of Transportation and Development
Louisiana Transportation Research Center

August 2026

Abstract

Additive Friction Stir Deposition (AFSD) is an emerging solid-state additive manufacturing process with significant potential for manufacturing, remanufacturing, and repairing transportation and civil infrastructure components. The process uses frictional heating, pressure, and severe plastic deformation to deposit metallic materials without bulk melting. This solid-state approach can reduce fusion-related defects, residual stresses, and material waste while producing dense deposits with refined microstructures. However, the application of AFSD to stainless steel remains challenging because of its high strength, work-hardening behavior, and resistance to plastic flow. This project develops an integrated computational framework to study the thermomechanical behavior of stainless steel during AFSD. The primary process-scale component is a Coupled Eulerian–Lagrangian (CEL) finite element model of AISI 316L stainless steel. The model evaluates temperature, stress, and material flow under different material and processing conditions. Molecular dynamics (MD) simulations were also conducted to provide fundamental insight into the deformation behavior that is not directly available from continuum modeling. The MD work included tensile and shear deformation of a stainless-steel-relevant Fe–Ni–Cr alloy, with particular attention to the influence of ultrasonic vibration. The tensile MD simulations showed that vibration changed the apparent stiffness, maximum stress, kinetic energy, and internal pressure of the alloy in a nonlinear manner. The shear simulations showed that vibration reduced mean shear stress in both the elastic and flow-stress regions. Defect analysis further indicated that vibration modified dislocation initiation, rearrangement, and annihilation. The CEL model predicted thermal and mechanical responses during stainless-steel deposition and showed good agreement with published experimental peak-temperature data. The model also demonstrated that constitutive parameters, tool rotational speed, traverse speed, and material deposition rate strongly influence predicted temperature, stress, and material flow. These results provide the foundation for future physics-informed machine learning, extended FE modeling, experimental validation, and process optimization for stainless-steel AFSD. Because sufficiently large and consistent stainless-steel AFSD process–response datasets were unavailable, the physics-informed machine learning methodology was developed and validated using laser powder bed fusion data for Ti-6Al-4V. The interaction-based conditional variational autoencoder achieved R^2 values of 0.955 for the full dataset and 0.870 for an 80/20 train–test split, outperformed conventional regression and neural-network models, and demonstrated transferable forward and inverse prediction capabilities that can be retrained using future AFSD datasets without modifying the model architecture.

Acknowledgements

The work was mainly supported by the Louisiana Transportation Research Center (LTRC) through Project number 26-3TIRE under State Contract number DOTLT1000592 and was funded in part by U.S. National Science Foundation under Grant Number OIA-2437963 and the Louisiana Board of Regents. The authors also acknowledge partial support from the Louisiana Board of Regents under Contract number LEQSF (2023–26)-RD-A-19, Program: R&D, Research Competitiveness Subprogram (RCS), and the National Science Foundation through cooperative agreement OIA-1946231 and Louisiana Board of Regents for the Louisiana Materials Design Alliance (LAMDA). Although not fully supported, Mr. Md Ashfaq Siddiquee, a Ph.D. student from the PI's group contributed to the project with the finite element modeling.

Implementation Statement

The computational framework developed in this project is intended to support the future implementation of AFSD for manufacturing and repairing stainless-steel transportation and civil infrastructure components. The CEL model provides a method for evaluating the effects of tool rotational speed, traverse speed, material deposition rate, material properties, and thermal conditions before extensive experimental testing is performed. This capability can help reduce trial-and-error experimentation and identify processing conditions that promote sufficient plasticization and stable material deposition.

The molecular dynamics simulations complement the process-scale model by providing fundamental insight into deformation resistance, internal stress, atomic rearrangement, and defect evolution. The MD results are not intended to directly replace experimental material properties or process-scale simulations. Instead, they provide mechanistic information that can help interpret FE predictions and guide future constitutive-model development.

The physics-informed machine learning component was implemented as a transferable methodology rather than as a stainless-steel predictive tool. Because AFSD process-response data for stainless steel are not yet available in sufficient quantity or consistency, the framework was developed and validated using laser powder bed fusion data for Ti–6Al–4V. The resulting interaction-based conditional variational autoencoder performs forward prediction of geometric response from process parameters and inverse estimation of process parameters from a target geometry, and it does so under limited-data conditions. These are the same capabilities that AFSD process selection will require. Implementation of this component consists of retraining the existing architecture on AFSD data, using tool rotational speed, traverse speed, and material deposition rate as inputs and deposited-layer geometry as the response. The model structure, training procedure, and evaluation approach do not need to be redeveloped.

The dataset required for this retraining consists of paired process settings and measured deposit responses collected under controlled conditions. The MELD L3 experimental campaign recommended in this report is the intended source. Each record should include tool rotational speed, traverse speed, material deposition rate, substrate preheat condition, and the corresponding measured deposited-layer width and height, peak temperature, and thermal history. CEL model results can supplement the experimental records and extend coverage of the parameter space where physical testing is impractical.

After the AFSD dataset is generated, the machine learning model is retrained on it, and the experimental-validation component is completed, the integrated framework may be used to screen processing conditions and support future AFSD applications involving bridge components, rail systems, pipelines, transportation equipment, and other metallic infrastructure.

Table of Contents

List of Tables

List of Figures

Introduction

Additive manufacturing has created new opportunities for producing and repairing metallic components while reducing material waste and enabling complex geometries. However, conventional fusion-based additive manufacturing processes involve repeated melting and solidification. These thermal cycles can produce porosity, cracking, distortion, residual stress, and microstructural nonuniformity. These issues are important for transportation and civil infrastructure because repaired or manufactured components must maintain reliable long-term performance.

Additive Friction Stir Deposition is a solid-state additive manufacturing process derived from friction-stir-based material processing. In AFSD, a rotating tool generates frictional heat and severe plastic deformation, causing the feedstock material to soften and consolidate onto a substrate without bulk melting. Because material bonding occurs in the solid state, AFSD can reduce defects associated with solidification and can produce dense deposits with refined, equiaxed grains and wrought-like properties [1][1].

AFSD has primarily been investigated for aluminum, magnesium, and other relatively soft materials [2]. Thermomechanical modeling has also been used to study the influence of rotational speed, traverse speed, and material deposition rate on aluminum-alloy AFSD [3]. However, the direct application of these findings to stainless steel is limited because stainless steel has higher strength, greater deformation resistance, and stronger work-hardening behavior.

The need for improved manufacturing and repair methods is especially important for transportation infrastructure. According to the project problem statement, 12.2% of Louisiana bridges are structurally deficient, compared with a national average of 6.8% [4]. Corrosion and fatigue-related damage are also major concerns for U.S. rail systems [5]. Steel remains a primary material for bridges, rail components, pipelines, vehicles, and other infrastructure systems, with U.S. steel consumption reaching approximately 98 million metric tons in 2021 [6].

Traditional repair methods such as welding, bolting, component replacement, and patching can restore damaged structures, but they may introduce residual stress, heat-affected regions, additional joints, or geometric limitations. AFSD offers an alternative approach in which material can potentially be deposited directly onto a damaged or worn region without melting the underlying structure. This capability may be valuable for

restoring corroded surfaces, rebuilding worn regions, adding reinforcing material, and remanufacturing high-value components.

AISI 316L stainless steel is widely used because of its strength, ductility, corrosion resistance, and thermal stability [7]. However, these properties also make the material difficult to process through AFSD. Stable stainless-steel deposition requires sufficient heat and mechanical energy to reduce deformation resistance while maintaining the solid-state nature of the process. Insufficient plasticization can cause poor bonding and material starvation, while excessive heat or material input can cause overflow, distortion, oxidation, or unstable deposition.

The original focus of this project was the development of a CEL-based finite element model and a physics-informed machine learning framework for stainless-steel AFSD. As the FE modeling progressed, the PI's group identified a need for more fundamental material information. The FE model uses continuum constitutive relationships, but these relationships do not directly explain the atomic origins of deformation resistance, internal stress redistribution, or defect evolution. The predictions were also found to depend strongly on the selected material-model parameters.

The PI's group therefore expanded the project to include molecular dynamics simulations. The atomistic work was not intended to reproduce the complete AFSD process. Instead, it was used to study the fundamental tensile and shear response of a stainless-steel-relevant Fe–Ni–Cr alloy. Tensile deformation provided a controlled method for evaluating apparent stiffness, maximum stress, kinetic energy, and pressure. Shear deformation was subsequently studied because material flow beneath the AFSD tool is primarily controlled by severe plastic deformation and shear.

A second adjustment was required for the physics-informed machine learning component. The original plan was to train a PIML model to predict thermomechanical properties of stainless steel from AFSD process conditions. A model of this type requires a dataset that links process inputs to measured responses across a range of conditions. No such dataset currently exists for stainless steel AFSD. Published studies report a small number of processing conditions and use different tool geometries, feedstock forms, and measurement methods, so the available results cannot be combined into a single consistent training set. The MELD L3 experiments intended to generate this data for the present framework were not completed within the project period. Training a model under these conditions would have produced predictions that could not be meaningfully validated.

The PIML methodology was therefore developed and demonstrated on laser powder bed fusion of Grade-5 Ti–6Al–4V, for which a large and consistently reported dataset is available. LPBF and AFSD differ fundamentally in their physics, since LPBF involves melting and solidification while AFSD is a solid-state process. The machine learning problem, however, has the same structure in both cases. A small number of process parameters interact nonlinearly to determine a thermally governed geometric response, the available data are limited relative to the size of the parameter space, and the inverse problem of selecting process settings to achieve a target geometry is non-unique. The interaction-based conditional variational autoencoder developed in this project addresses these specific features and is formulated in terms of process parameters and geometric responses rather than melting physics. Substituting tool rotational speed, traverse speed, and material deposition rate for laser power, scanning speed, and layer thickness, and deposited-layer geometry for melt-pool geometry, leaves the architecture unchanged. The LPBF study therefore establishes and validates the methodology so that it can be retrained rather than redeveloped once AFSD data become available.

The overall project combines three complementary approaches. MD provides atomic-scale insight into material deformation and defects. CEL finite element modeling predicts process-scale temperature, stress, and material flow. Physics-informed machine learning connects process parameters to material response under physical constraints, and the framework validated in this project provides the method for linking computational and experimental AFSD data once that data are collected.

Literature Review

AFSD has received increasing attention as a solid-state route for additive manufacturing and repair. Yu and Mishra described AFSD as a deformation-processing route in which metallic feedstock is consolidated through frictional heating and plastic flow without melting [1]. This processing route can reduce solidification-related defects and produce refined microstructures.

Most early AFSD investigations focused on aluminum and other relatively soft alloys. Mason et al. studied the process–structure–property relationships of solid-state additively manufactured high-strength aluminum and showed that processing conditions strongly influence the resulting material response [2]. Alam et al. used thermomechanical modeling to investigate aluminum-alloy AFSD and demonstrated that rotational speed, traverse speed, and deposition rate affect temperature, stress, and material flow [3].

The use of stainless steel in AFSD has received less attention. Agrawal et al. investigated AFSD of SS316 and reported process-dependent recrystallization and ultrafine equiaxed grains [8]. Gor et al. demonstrated AFSD of super duplex stainless steel and reported refined microstructures with promising mechanical properties [9]. These studies confirm the feasibility of stainless-steel AFSD but also show that process control is more difficult than for lower-strength alloys.

Numerical modeling is important because temperature, stress, and material flow are difficult to measure directly beneath the rotating tool. Stubblefield et al. developed a meshfree computational framework for AFSD and showed that numerical modeling can capture severe deformation and material movement during deposition [10]. CEL modeling has also been used in friction-stir-based processes because it combines Lagrangian components with an Eulerian material domain. Al-Badour et al. demonstrated that CEL modeling can represent tool motion, material flow, heat generation, and deformation during friction stir welding [11].

Physics-informed machine learning offers an additional method for improving material and process predictions when experimental data are limited. Peng et al. coupled physical knowledge with machine learning to predict high-temperature alloy properties [12]. Du et al. discussed the integration of mechanistic modeling and physics-informed machine learning for reducing defects in additive manufacturing [13]. These studies provide the basis for using physical constraints together with computational and experimental data.

The PI's group also conducted molecular dynamics simulations to investigate the behavior of stainless-steel-relevant Fe–Ni–Cr alloys. The tensile study showed that ultrasonic vibration changed the apparent modulus, maximum stress, kinetic energy, and internal pressure in a parameter-dependent manner [14]. The later shear study showed that vibration reduced mean shear stress and modified dislocation evolution under deformation conditions more closely related to AFSD material flow [15].

The FE work developed by the PI's group used a CEL framework to model AISI 316L stainless-steel deposition. The model incorporated temperature-dependent material properties, Johnson–Cook plasticity, frictional contact, and different process conditions [16]. Together, the MD and FE studies provide material-scale and process-scale information for the broader integrated computational framework.

Physics-Informed Machine Learning

Physics-informed machine learning integrates physical knowledge with data-driven models to improve prediction accuracy and generalization, particularly when experimental data are limited. In metal additive manufacturing, these approaches have been used to model temperature evolution, melt-pool geometry, and nonlinear process–material relationships.

Jiang et al. developed a physics-informed machine-learning framework to predict temperature and melt-pool dimensions under different processing conditions [18]. Peng and Panesar applied a physics-informed neural network to multilayer thermal simulation, demonstrating that governing physics can be embedded directly into the learning process [19]. Li et al. introduced statistical parameterized physics-based machine-learning digital-shadow models for LPBF, combining mechanistic information with data-driven prediction [20]. Similarly, Mathew et al. developed a physics-informed intelligent framework for geometric prediction and compensation in metal additive manufacturing [21].

Building on these developments, Shuvo et al. proposed a physics-inspired Conditional Variational Autoencoder that captures nonlinear interactions between process parameters and melt-pool geometry [17]. The model used interaction-based features instead of conventional input concatenation and enabled both forward geometry prediction and inverse process-parameter estimation. The numerical model achieved an overall R2R^2R2 of 0.955 using the full dataset and 0.870 under an 80/20 train-test split.

Although these studies primarily focused on LPBF, their underlying methodologies are applicable to AFSD. Rotational speed, traverse speed, deposition rate, temperature, and material properties interact nonlinearly during AFSD. Therefore, physics-informed

machine learning can integrate molecular dynamics, CEL finite element, and experimental data to predict thermomechanical behavior and support process-parameter optimization.

Objective

The overall objective of this study is to develop a CEL-based finite element model that can reliably predict the thermal behavior and material flow associated with plastic deformation of stainless steel during Additive Friction Stir Deposition.

The specific objectives are:

1. Predict selected thermomechanical properties of 316 stainless steel using physics-informed machine learning.

2. Develop a CEL model for the AFSD process incorporating temperature-dependent stainless-steel properties.

3. Optimize major process parameters, including tool rotational speed, traverse speed, and material deposition rate, based on temperature response and deposited-layer geometry.

4. Validate the CEL model by comparing its predictions with experimental results obtained from published studies and future MELD L3 experiments.

5. Use molecular dynamics simulations to provide fundamental insight into tensile deformation, shear deformation, vibration-assisted deformation, and defect evolution in a stainless-steel-relevant Fe–Ni–Cr alloy.

6. Develop an integrated computational framework linking atomic-scale behavior, finite element modeling, machine learning, and experimental validation.

Scope

The scope of this project includes molecular dynamics modeling, Coupled Eulerian–Lagrangian finite element modeling, physics-informed machine learning, and experimental validation.

The molecular dynamics task examines the fundamental deformation behavior of a stainless-steel-relevant Fe–Ni–Cr alloy. The PI's group investigated tensile and shear deformation with and without ultrasonic vibration. The tensile study focused on apparent stiffness, maximum stress, kinetic energy, and internal pressure. The shear study focused on shear resistance, flow stress, atomic rearrangement, and dislocation evolution. The MD analysis provides information that cannot be directly obtained from a conventional continuum model.

The finite element task focuses on the development of a CEL model for single-layer AFSD of AISI 316L stainless steel. The model represents the tool, actuator, feedstock, substrate, frictional contact, plastic deformation, heat generation, and material movement. It is used to evaluate the effects of material properties and processing conditions on temperature, stress, flow, and deposition behavior.

The physics-informed machine learning task will combine physical constraints with computational and experimental data. The objective is to develop an accurate predictive model while reducing reliance on extensive experimental testing. The detailed FE–machine learning methodology will be completed separately by the PI.

The expected outcomes and deliverables include:

- Development of a high-accuracy PIML model for predicting thermomechanical properties of stainless steel.
- Reduced experimental dependency through data-driven analysis and extended FE modeling.
- Provision of missing material information for improved CEL and FE modeling of AFSD.
- Development of an efficient integrated computational framework for advanced materials and manufacturing processes.

- Identification of important material and process parameters for stainless-steel AFSD.
- Establishment of a technical basis for future experimental validation and infrastructure applications.

Methodology

Integrated Computational Approach

The PI's group used atomistic and continuum modeling to study different parts of the stainless-steel AFSD problem. The MD simulations were used to examine fundamental deformation and defect behavior. The CEL model was used to predict temperature, stress, and material flow during deposition. The physics-informed machine learning component will later combine model predictions and experimental information.

The atomic-scale analysis was added because the FE model requires constitutive material information but does not directly explain the physical mechanisms responsible for deformation resistance and material softening. The MD work therefore provides supporting insight rather than a direct simulation of the complete AFSD process.

Molecular Dynamics Analysis

The PI's group modeled a $Fe_{60}Ni_{20}Cr_{20}$ random solid solution with an FCC crystal structure. The system contained 13,500 atoms and used periodic boundary conditions to represent bulk-like material behavior. Simulations were conducted using LAMMPS, and atomic interactions were described using Fe–Ni–Cr Modified Embedded Atom Method potentials [14], [15].

Table 1. Summary of the Molecular Dynamics Simulations

Model feature	Tensile study	Shear study
Alloy composition	$Fe_{60}Ni_{20}Cr_{20}$	$Fe_{60}Ni_{20}Cr_{20}$
Crystal structure	FCC random solid solution	FCC random solid solution
Number of atoms	13,500	13,500
Boundary condition	Periodic in all directions	Periodic in all directions
Temperature	300 K	1 K
Strain rate	0.001 ps^{-1}	0.001 ps^{-1}

Loading condition	Uniaxial tension	Simple shear in the xy plane
Vibration amplitudes	1, 2, and 5 Å	0.3–0.6 Å depending on deformation region
Vibration frequencies	0.1–10 GHz	0.5–1.5 THz
Main quantities evaluated	Apparent modulus, maximum stress, kinetic energy, and pressure	Mean shear stress, acoustic softening, defects, and dislocations

The tensile simulations were conducted first without vibration to establish a baseline. Ultrasonic vibration was then applied to atomic slab groups using a sinusoidal displacement:

$$x(t) = A\cos\left(2\pi f t - \frac{x_c}{\lambda}\right) \quad (1)$$

where A is the vibration amplitude, f is the frequency, x_c is the slab-center position, and λ is the effective wavelength. Fifteen combinations of amplitude and frequency were investigated. The tensile analysis focused on changes in stress response, apparent Young's modulus, maximum stress, kinetic energy, and internal pressure.

Figure 1. Atomistic Fe–Ni–Cr simulation system under (a) tensile loading only and (b) tensile loading with ultrasonic vibration

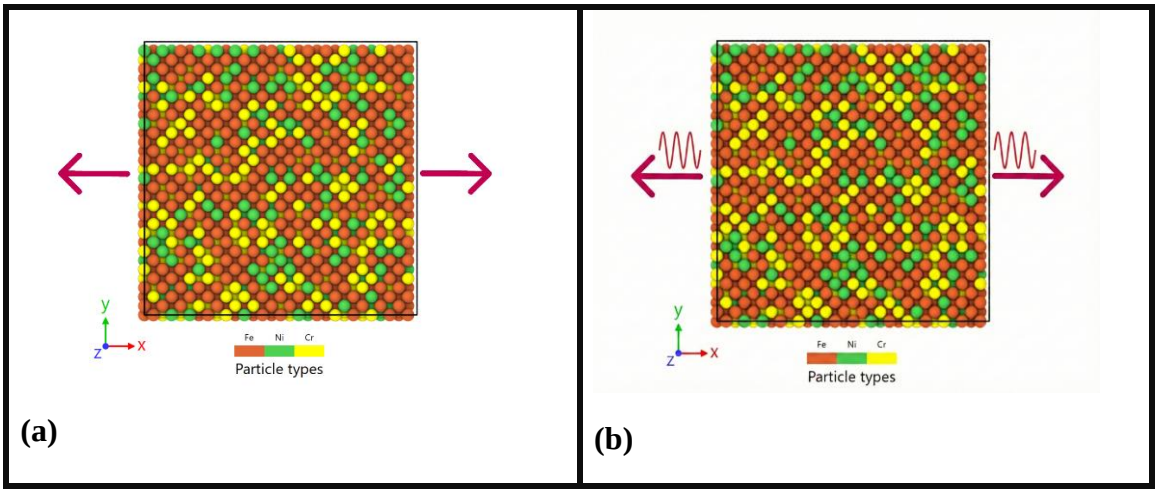

The shear simulations were conducted at 1 K to reduce thermal softening and isolate the mechanical effect of vibration. Simple shear was applied in the xy plane. Ultrasonic vibration was imposed in the x direction with a phase variation along the y direction:

$$u_x(y,t) = A\cos[\omega t - k(y - y_0)] \quad (2)$$

where A is the amplitude, ω is the angular frequency, k is the wave number, and y_0 is the center of the simulation cell.

A three-stage procedure was used. The alloy was first sheared without vibration, then sheared while vibration was applied, and finally sheared again after vibration was removed. This approach allowed direct comparison before, during, and after vibration along the same deformation path.

Figure 2. Three-stage acoustic-softening protocol used in the shear simulations: (a) shear only, (b) shear with ultrasonic vibration, and (c) shear after vibration removal

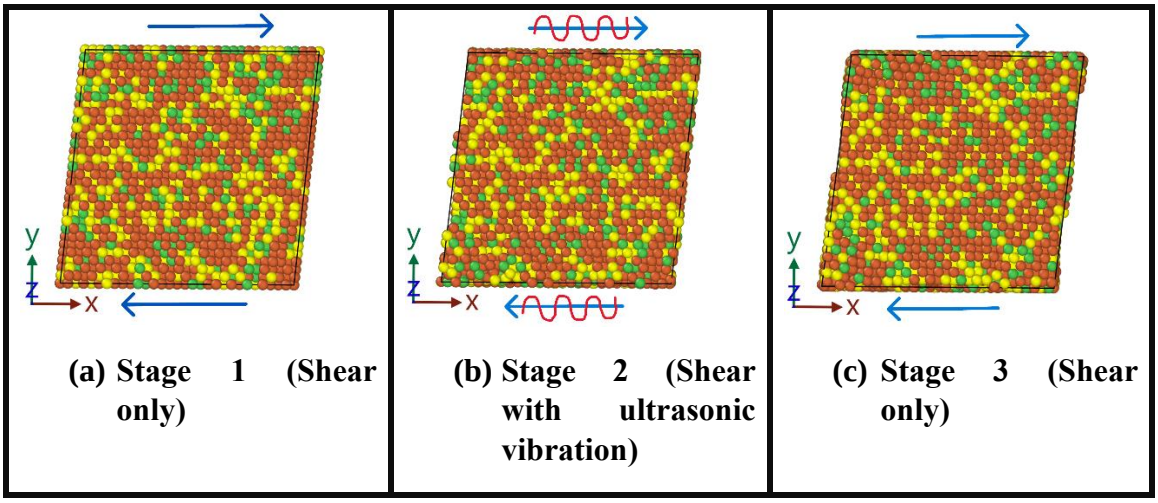

(a) Stage 1 (Shear only) **(b) Stage 2 (Shear with ultrasonic vibration)** **(c) Stage 3 (Shear only)**

Because vibration created an oscillatory stress response, acoustic softening was evaluated using the mean stress during the vibration period:

$$\Delta\bar{\tau}_{\mathrm{USV}} = \bar{\tau}_{\mathrm{base}} - \bar{\tau}_{\mathrm{vib}} \quad (3)$$

where $\bar{\tau}_{\mathrm{base}}$ is the mean baseline stress and $\bar{\tau}_{\mathrm{vib}}$ is the mean vibration-assisted stress over the same strain range.

Atomic configurations from the shear simulations were analyzed using OVITO and the Dislocation Extraction Algorithm. The main quantities examined were dislocation count and total dislocation line length.

Coupled Eulerian–Lagrangian Finite Element Analysis

The FE model was developed in Abaqus using a CEL formulation. CEL was selected because the AFSD process involves severe deformation and continuous material

movement. The tool and actuator were represented using Lagrangian components, while the highly deforming material was modeled within an Eulerian domain.

The model included an AISI 316L stainless-steel feedstock, stainless-steel substrate, hollow circular tool, and rigid actuator. The substrate measured 120 mm by 80 mm by 10 mm. The cylindrical feedstock had an outer diameter of 28 mm and an inner diameter of 20 mm. Frictional contact between the rotating tool and feedstock generated heat and caused the stainless steel to deform and flow onto the substrate.

Figure 3. CEL model showing the Eulerian space, substrate, feed material, rotating tool, and actuator

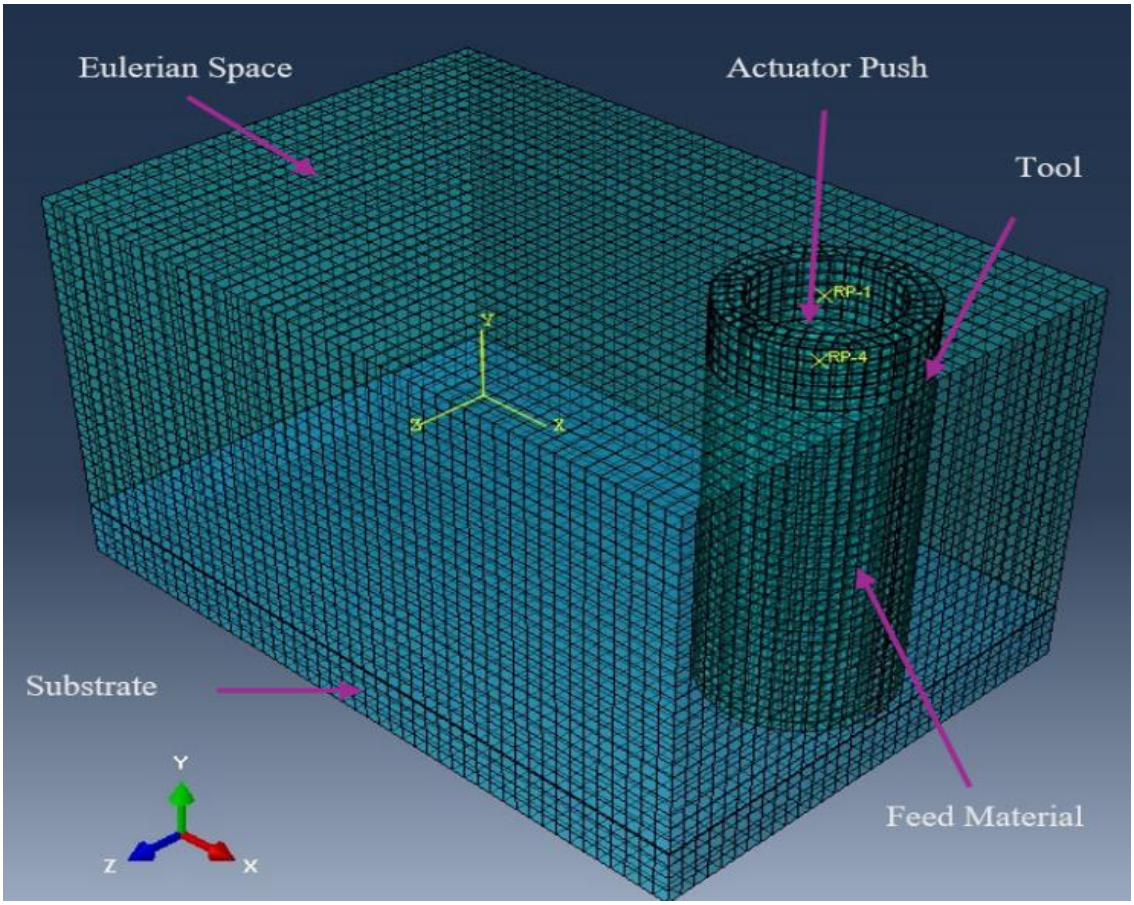

Temperature-dependent heat capacity, thermal conductivity, density, and Young's modulus were assigned to the stainless steel. Plastic behavior was represented using the Johnson–Cook model:

$$\sigma_y = \left(A + B\varepsilon_p^n\right)\left[1 + C\ln\left(\frac{\dot{\varepsilon}_p}{\dot{\varepsilon}_0}\right)\right](1 - T^{*m}) \qquad (4)$$

where A, B, C, n, and $m$are material constants, $\varepsilon_p$is the equivalent plastic strain, $\dot{\varepsilon}_p$ is the plastic strain rate, and T^* represents normalized temperature.

The FE study evaluated multiple literature-based Johnson–Cook parameter sets because the predicted behavior was sensitive to the selected material constants. The model also included frictional contact and thermal boundary conditions.

Table 2. Main CEL Model Inputs

Model input	**Value or description**
Analysis software	Abaqus
Modeling method	Coupled Eulerian–Lagrangian
Feedstock material	AISI 316L stainless steel
Substrate material	AISI 316L stainless steel
Substrate dimensions	120 mm × 80 mm × 10 mm
Feedstock outer diameter	28 mm
Feedstock inner diameter	20 mm
Friction coefficient	0.5
Air temperature	25°C
Substrate–air heat transfer coefficient	15 W/m²°C
Base temperature	200°C
Substrate–base heat transfer coefficient	4 W/m²°C
Plasticity model	Johnson–Cook
Main outputs	Temperature, equivalent stress, material flow, and deposited-layer behavior

A mesh-convergence study was conducted using three mesh sizes. The predicted peak temperature changed substantially between the coarse and medium meshes but only slightly after further refinement. The final analysis used a mesh-converged model consisting of Eulerian, deformable-solid, and rigid elements.

The CEL model was initially validated using published experimental data for AFSD of SS316. The validation condition used a rotational speed of 800 rpm, a traverse speed of 4.23 mm/s, and a material deposition rate of 0.42 mm/s. The experimental and predicted peak temperatures were compared to evaluate the model's thermal accuracy.

Physics-Informed Machine Learning

The physics-informed machine learning task was originally planned for stainless steel AFSD. That task requires a dataset linking process inputs to measured responses across a range of conditions, and no dataset of this kind is currently available for stainless steel AFSD. Published AFSD studies cover a limited number of processing conditions and use inconsistent tool geometries, feedstock forms, and measurement procedures, so the reported results cannot be pooled into a single training set. The MELD L3 experiments that will supply this data were not completed within the project period. The methodology was therefore developed and validated on laser powder bed fusion of Grade-5 Ti–6Al–4V, which was selected because it presents the same modeling problem in a data-rich setting. Both processes involve a small number of process parameters that interact nonlinearly, a thermally governed geometric response, limited data relative to the size of the parameter space, and a non-unique inverse mapping. The framework described in this section is formulated in terms of process parameters and geometric responses rather than melting physics, so the same architecture can be retrained on AFSD data when it becomes available.

Physics-informed machine learning (PIML) integrates machine learning with physical knowledge so that predictions are guided by both data patterns and process mechanisms. In additive manufacturing, this is useful because melt-pool behavior is controlled by nonlinear thermal and fluid-flow effects, while experimental data are often limited and expensive to obtain [18–21].

The material considered in this task is Grade-5 Ti–6Al–4V (Ti64). During LPBF, Ti64 powder is locally melted and rapidly solidified; therefore, its effective density, heat capacity, thermal conductivity, viscosity, and surface tension directly affect heat absorption, melt-pool flow, and final melt-pool geometry.

Data Collection

The data collection procedure involved recording LPBF process conditions, measuring the corresponding melt-pool geometry from calibrated cross-sectional images, and organizing the processed data for numerical and image-based modeling. For each experimental condition, the available process parameters and melt-pool responses were collected and consolidated.

The process parameters included laser power (*P*), scanning speed (*v*), powder-layer thickness (l_t), laser spot diameter (*d*), and initial powder-bed porosity (φ). The melt-pool responses were maximum width (*W*), maximum depth (*D*), and the cross-sectional melt-pool image (*I*). In this study, porosity refers to the void fraction in the powder bed before laser exposure, not the final porosity of the deposited track. It is defined as:

$$\varphi = \left(1 - \frac{\rho_{sample}}{\rho_{solid}}\right) \times 100$$

where ρ_{sample} is the effective powder-bed density and ρ_{solid} is the theoretical density of fully dense Ti–6Al–4V.

Based on the available data, two task-specific datasets were created.

i) The numerical dataset contains the process parameters with the corresponding melt-pool width and depth measurements. It initially included 830 samples, and 810 valid samples were retained after removing zero-valued records. The parameter ranges used in the numerical dataset are summarized in Table 3. These ranges cover the main LPBF operating window considered in this study and include both input process parameters and measured melt-pool responses.

Table 3. Parameter ranges for Dataset 1

Parameter	Min	Max
P [W]	50	520
v [mm/s]	0	3200
d [μm]	30	250
l_t *[μm]*	58	140
φ [%]	0	57.6
W [μm]	45	415.5
D [μm]	5	980

ii) The image dataset consists of 23 calibrated melt-pool cross-sectional images with their corresponding process parameters, width, and depth. The numerical dataset was used for forward geometry prediction and reverse modeling, while the image dataset was used for image-based and hybrid digital-twin development.

Data Preprocessing

The collected numerical and image data were preprocessed to ensure consistency before model development. The numerical records were first screened for missing values, duplicate entries, zero-valued records, and nonphysical parameter-response combinations.

Since the data were obtained from multiple sources, only records collected under comparable LPBF operating conditions and measurement procedures were retained. The cleaned numerical variables were then normalized using min-max scaling before being used in the learning models.

Figure 4. Geometry calibration and representative melt-pool measurement workflow: (a) pixel-to-micron calibration using a 150 () scale bar and (b) a representative cross section used for geometry extraction [17].

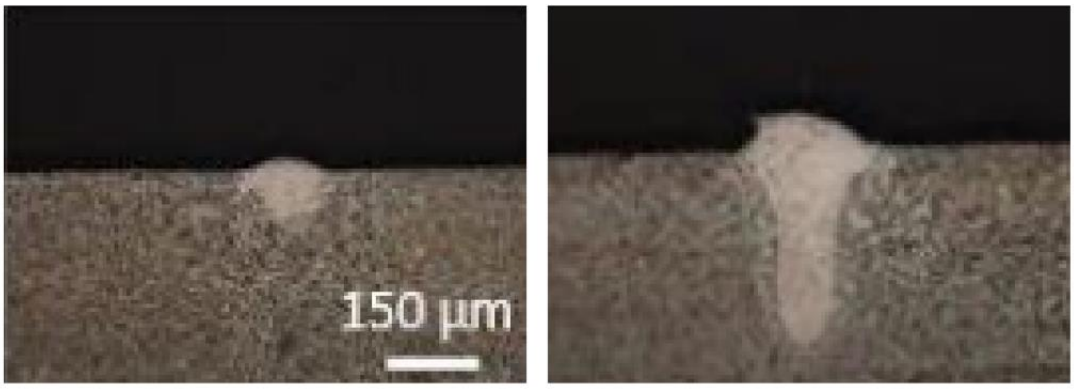

(a) Pixel-to-micron calibration using a 150 μm reference scale bar.

(b) Representative melt-pool cross section used for geometry extraction.

For the image dataset, the preprocessing procedure followed the calibration workflow shown in Figure 4. A reference image with a 150 µm scale bar was used to determine the pixel-to-micron conversion factor. The measured scale-bar length was 24.130 pixels, corresponding to 6.21 µm/pixel. This calibration factor was applied consistently to the cross-sectional images to extract melt-pool width and depth. The melt-pool boundary was identified using FIJI/ImageJ and further refined through Python-based segmentation and validation. Finally, the images were cropped around the melt-pool region, converted to grayscale, normalized, and resized to 128 × 128 pixels.

Physics-Inspired Formulation of Melt-Pool Modeling

LPBF uses a high-intensity moving laser to melt selected regions of a powder bed. Melt-pool formation is governed by transient heat conduction, laser-energy absorption, phase-dependent thermophysical properties, momentum transfer, and surface-tension-driven fluid flow. In a moving coordinate system, the temperature field $T(x, t)$ is described by the transient energy-conservation relationship:

$$\rho_{\text{eff}} c_{p,\text{eff}} \left(\frac{\partial T}{\partial t} + v \frac{\partial T}{\partial y} \right) = \nabla \cdot (k_{\text{eff}} \nabla T) + \dot{q}(x, t) \qquad (4)$$

where ρ_{eff}, $c_{p,\text{eff}}$, and k_{eff} are the effective density, effective specific heat capacity, and thermal conductivity of the powder-substrate system; v is the laser scanning speed; and

$\dot{q}(x,t)$ is the volumetric heat source. The absorbed laser energy may be approximated using a Gaussian volumetric heat-source distribution:

$$\dot{q}(r,z) = \frac{2\eta P}{\pi d^2}\exp\left(-\frac{2r^2}{d^2}\right)f(z) \qquad (5)$$

where (P) is laser power, (d) is the beam diameter, (η) is laser absorptivity, (r) is the radial distance from the beam center, and ($f(z)$) accounts for attenuation through the powder layer. The combined effect of laser power, scanning speed, spot diameter, and layer thickness is represented by the volumetric energy-density descriptor:

$$E = \frac{\eta P}{v d l_t} \qquad (6)$$

Melt-pool width (W) and depth (D) correspond approximately to the melting-temperature isotherm. During melting, temperature gradients along the free surface generate Marangoni shear stress, which drives fluid flow and strongly affects melt-pool morphology:

$$\tau_s = -\frac{\partial \gamma}{\partial T}\frac{\partial T}{\partial s} \qquad (7)$$

where (γ) is surface tension, ($\frac{\partial \gamma}{\partial T}$) is its temperature coefficient, and ($\frac{\partial T}{\partial s}$) is the tangential temperature gradient along the liquid surface. These relationships explain why the selected process parameters affect melt-pool geometry through coupled thermal and fluid mechanisms.

A conventional forward mapping relates the process variables to the melt-pool responses through a learned, physically meaningful latent representation:

$$\{P, v, d, l_t, \phi\} \rightarrow \Phi\left(E, c_{p,\text{eff}}, k_{\text{eff}}, \rho_{\text{eff}}, \tau_s\right) \rightarrow \{W, D, I\} \qquad (8)$$

In the inverse direction, the melt-pool response is used to infer process settings capable of producing the prescribed geometry:

$$\{W, D, I\} \rightarrow \Psi\left(E, c_{p,\text{eff}}, k_{\text{eff}}, \rho_{\text{eff}}, \tau_s\right) \rightarrow \{P, v, d, l_t, \phi\} \qquad (9)$$

In Equations (8) and (9), ($\Phi(\cdot)$) and ($\Psi(\cdot)$) denote the learned forward and reverse mappings associated with energy input, effective heat capacity, thermal conductivity, effective density, and Marangoni shear stress. These physical quantities serve as theoretical descriptors. The implemented model uses the primary process variables directly to avoid feature redundancy and multicollinearity.

Figure 5. Bidirectional CVAE formulation connecting LPBF process variables, a physics-informed latent representation, and melt-pool geometry [17].

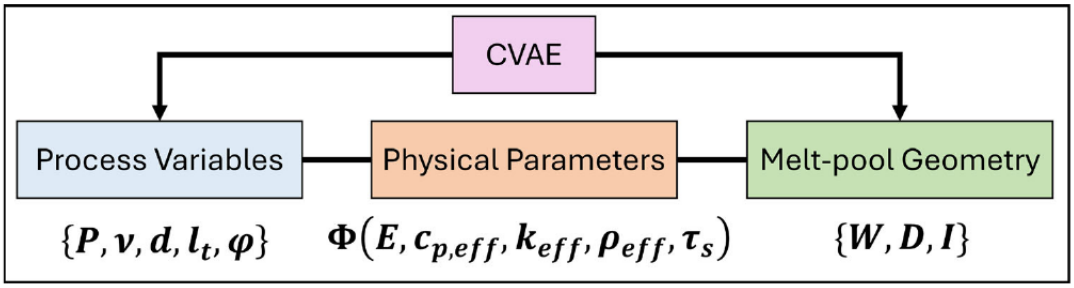

Physics-Informed Machine-Learning Framework

The proposed framework uses a Conditional Variational Autoencoder (CVAE) to learn the joint nonlinear relationships between LPBF inputs and melt-pool responses. The normalized process input vector is

$$\mathbf{x} = \{x_P, x_v, x_d, x_{l_t}, x_\phi\} \qquad (10)$$

and contains normalized laser power, scanning speed, spot size, layer thickness, and porosity. The normalized response vector is

$$\mathbf{y} = \{y_W, y_D, y_I\} \qquad (11)$$

where y_W, y_D and y_I represent normalized melt-pool width, depth, and image, respectively. Width and depth describe the global melt-pool geometry, while the image retains the spatial morphology of the fusion boundary.

Conditional Variational Autoencoder

During training, the CVAE encoder receives paired process and response data *(x, y)* and maps them to a latent probability distribution described by a mean (μ) and standard deviation (σ). A latent sample (z) is generated through the reparameterization procedure, and the conditional decoder reconstructs the target response using (z) together with the prescribed process variables. The training objective combines reconstruction error with Kullback-Leibler regularization so that the latent space remains continuous and can generate physically plausible samples.

During prediction, a latent sample is drawn from the learned prior and supplied to the decoder with the known process conditions. This generative formulation is appropriate because melt-pool formation is stochastic and because multiple process settings may produce similar geometries. Therefore, the CVAE supports both uncertainty-aware forward prediction and one-to-many inverse process design.

Interaction-Based CVAE

A conventional CVAE concatenates the input and output vectors before encoding. Under limited-data conditions, this requires the network to learn within-variable behavior and all cross-dependencies from an expanded, weakly structured feature space. The proposed interaction-based CVAE replaces simple concatenation with the outer product of the process and geometry variables:

$$\mathbf{x} \otimes \mathbf{y} = \begin{bmatrix} x_P y_W & x_v y_W & x_d y_W & x_{l_t} y_W & x_\phi y_W \\ x_P y_D & x_v y_D & x_d y_D & x_{l_t} y_D & x_\phi y_D \end{bmatrix} \qquad (18)$$

Equation (18) produces ten interaction terms. For example, $x_P y_W$ represents the interaction between laser power and melt-pool width, while $x_\phi y_D$ represents the interaction between porosity and melt-pool depth. The encoder receives this structured matrix and uses a neural network to estimate the underlying nonlinear, physics-like relationships. The latent representation stores the coupled parameter-geometry information in compact form, and the decoder combines this latent state with the process inputs to predict width and depth. This formulation reduces effective model complexity and improves learning efficiency when the available dataset is limited [17].

Digital-Twin Architectures

The complete bidirectional framework is constructed using four related architectures. Three models operate in the forward direction: the numerical digital twin predicts melt-pool width and depth from process parameters, the image-based digital twin reconstructs melt-pool cross-sectional images, and the hybrid digital twin combines numerical geometry prediction with image generation. The fourth model operates in the reverse direction, where the target melt-pool geometry is used to infer feasible process-parameter combinations. Together, these forward and reverse architectures enable both prediction of melt-pool responses and inverse design of LPBF processing conditions.

Numerical Digital Twin

The numerical digital twin predicts melt-pool width and depth from the five process parameters. During training, the encoder receives the interaction matrix ($x \otimes y$) and estimates μ and σ for the latent distribution. The decoder reconstructs (W) and (D) from the latent sample conditioned on (x). During inference, only the process variables and a latent sample are supplied to the decoder. This model provides a computationally efficient surrogate for melt-pool geometry prediction.

Figure 6. Interaction-based CVAE architecture used for the numerical digital twin [17].

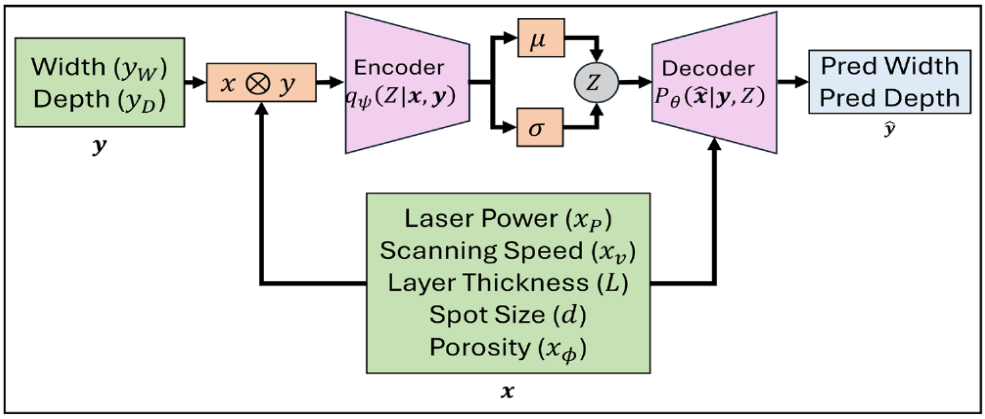

Image-Based Digital Twin

The image-based digital twin is implemented as a convolutional CVAE. During training, convolutional layers extract spatial features from the melt-pool image, which are combined with the associated process variables and geometry before latent encoding. The decoder uses transposed convolutions to reconstruct a (128) cross-sectional image. During prediction, the process conditions and a sampled latent vector are supplied to the decoder to synthesize a plausible melt-pool cross section.

Figure 7. Training and prediction phases of the image-based CNN-CVAE digital twin [17].

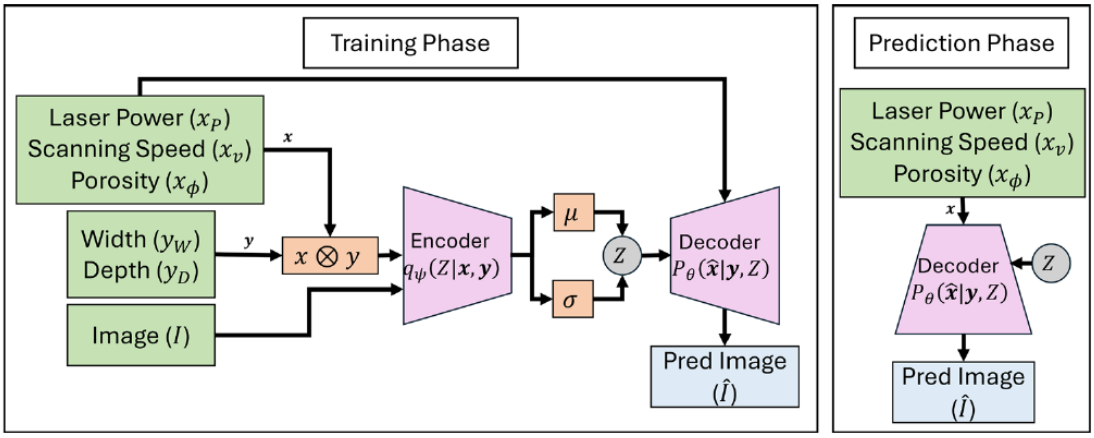

Hybrid Digital Twin

The hybrid digital twin links numerical geometry prediction with image reconstruction. Stage 1 predicts width and depth from the process settings using the numerical CVAE. Stage 2 receives the predicted geometry together with the same process variables and reconstructs a geometry-consistent melt-pool image. This two-stage design uses the larger numerical dataset to provide a physically interpretable link for the image model, which is trained using only 23 images.

Figure 8. Two-stage hybrid digital-twin architecture for geometry prediction and image reconstruction [17].

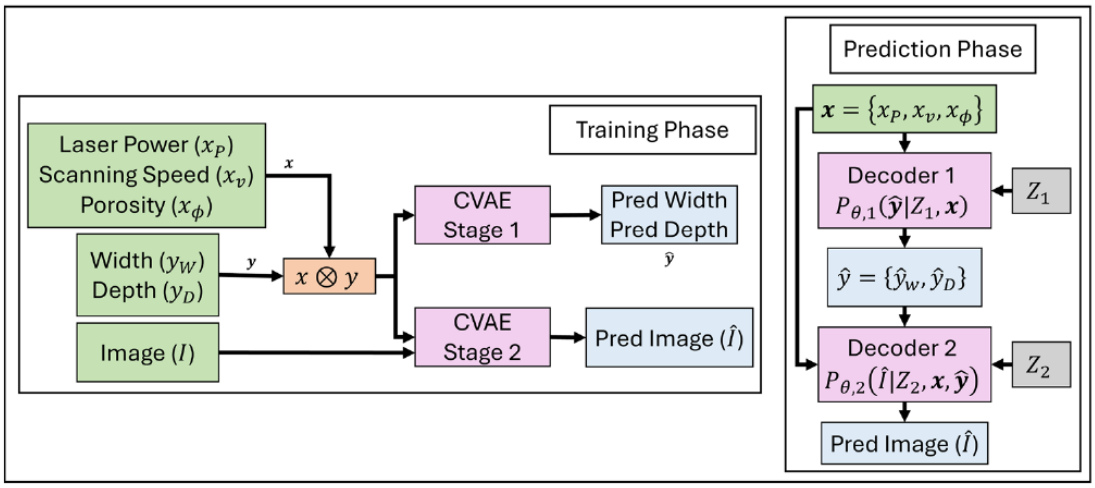

Reverse Digital Twin

The reverse digital twin extends the proposed framework from forward prediction to inverse process design. Instead of predicting melt-pool geometry from known process parameters, this architecture infers feasible process conditions from a desired melt-pool width and depth. During training, the encoder learns the coupled relationship between the process-parameter vector and the corresponding melt-pool geometry through the interaction-based representation. The decoder then reconstructs the process parameters by conditioning the latent state on the target geometry.

Figure 9. Reverse digital-twin architecture for geometry-conditioned inference of LPBF process parameters. Source: Shuvo et al. [17].

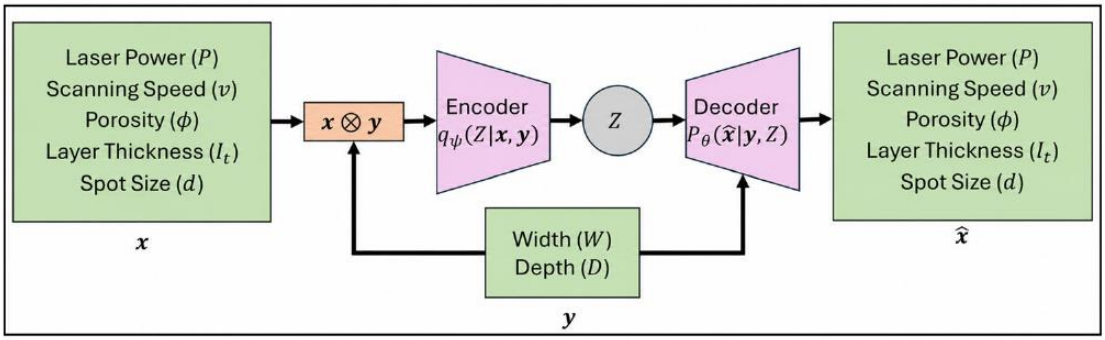

This reverse formulation is a key contribution of the study because the inverse mapping is inherently non-unique. Different combinations of laser power, scanning speed, layer thickness, spot size, and porosity can produce similar melt-pool geometries. Therefore, the model learns a conditional distribution of physically admissible process-parameter combinations rather than a single deterministic solution. This enables uncertainty-aware inverse design and provides a practical route for selecting process settings that can achieve a prescribed melt-pool response.

Coefficient of Variation

In this study, the coefficient of variation (CV) is used to interpret model performance relative to the natural variability of the dataset. This is important because the process parameters and melt-pool responses have different units, scales, and levels of dispersion. Some variables, such as spot size and porosity, have limited variation, so even small prediction differences can be significant, whereas variables with larger CV values can tolerate wider physically plausible deviations.

CV measures the relative spread of a variable with respect to its mean. For a population with mean μ and standard deviation σ:

$$\mathrm{CV} = \frac{\sigma}{|\mu|} \qquad (26)$$

For sample data, the corresponding estimate is

$$\widehat{\mathrm{CV}} = \frac{s}{|\bar{x}|} \qquad (27)$$

where $\bar{x}$ is the sample mean and s is the sample standard deviation. For reverse-model evaluation, the cleaned dataset is grouped using the melt-pool aspect ratio, R = D/W, into shallow-wide, balanced, and deep-narrow regimes. The regime-wise CV values are then used to judge whether prediction differences mainly reflect model error or the natural dispersion, limited variation, and sparsity of each melt-pool regime.

Discussion of Results

Tensile Molecular Dynamics Results

The baseline tensile simulation showed an elastic region followed by yielding, strain hardening, maximum stress, and post-peak softening. The apparent Young's modulus was approximately 182 GPa, and the maximum stress was approximately 19.5 GPa at a strain of about 0.21.

Ultrasonic vibration changed both the apparent modulus and maximum stress. The response was not directly proportional to amplitude or frequency. For the higher-amplitude cases, maximum stress increased as frequency approached 1 GHz and then decreased at higher frequencies. At the highest vibration conditions, the stress response became too noisy to calculate a consistent apparent modulus.

The kinetic-energy and pressure analysis showed that vibration increased the energy of the atomic system and changed internal stress distribution. However, pressure did not increase proportionally with kinetic energy at all conditions. This indicates that the atomic response to vibration was nonlinear

Figure 10. Summary of tensile MD results showing the (a) baseline response, (b) vibration-assisted response, (c) apparent modulus, (d) maximum stress, (e) kinetic energy, and pressure-field behavior

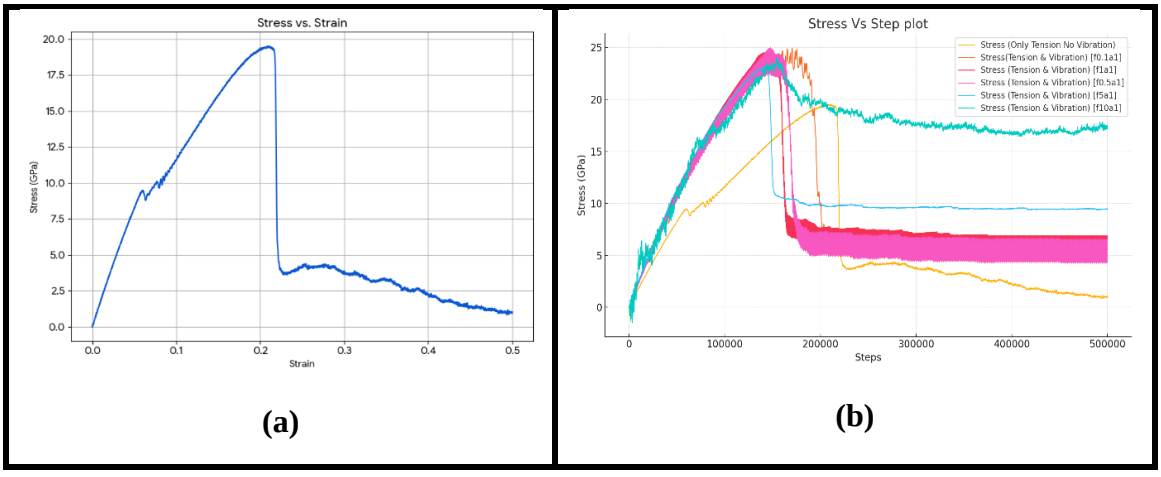

(a) **(b)**

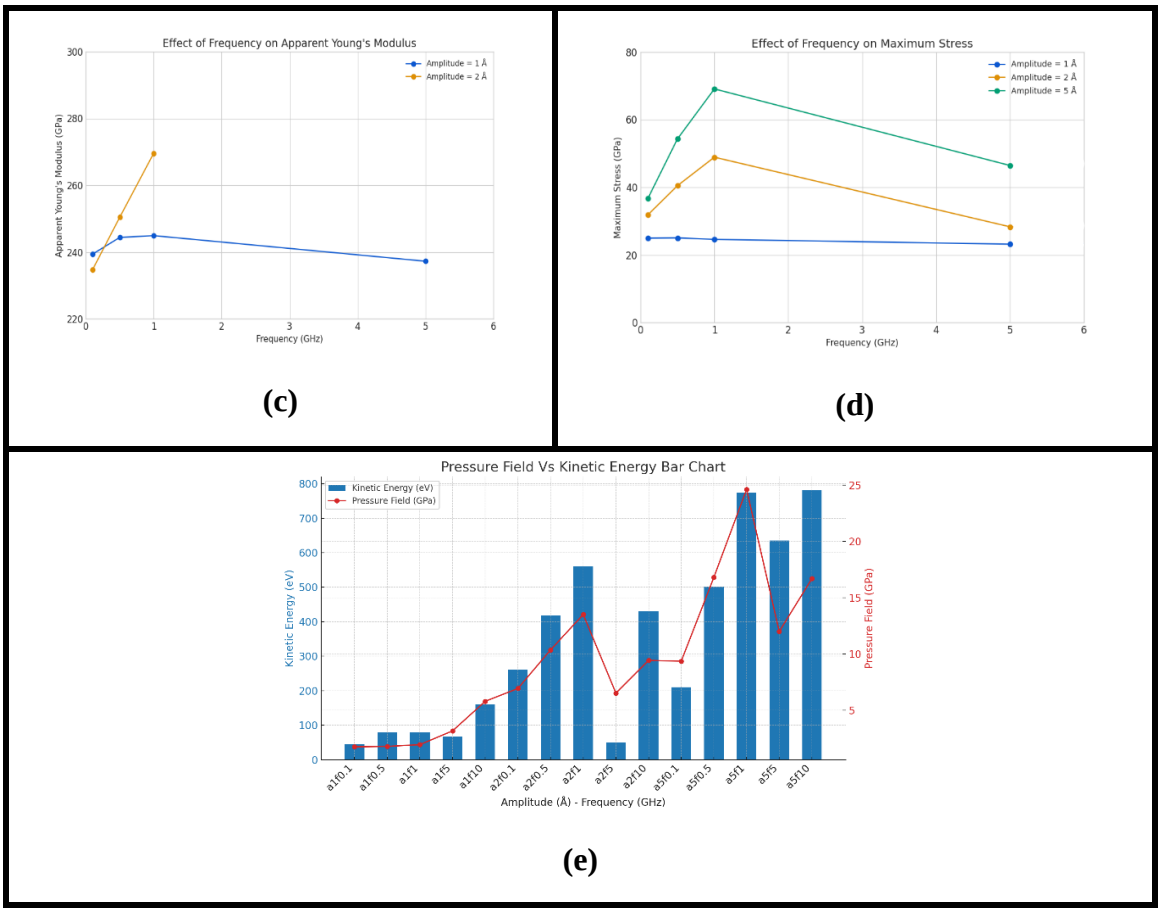

Shear Acoustic-Softening Results

The shear simulations showed a clear stress reduction during the vibration period. In the elastic shear region, all nine vibration-assisted cases produced a lower mean stress than the baseline. The reduction ranged from 16.41% to 37.23%. The response did not increase consistently with frequency, indicating that the elastic-region behavior depended on the combined amplitude and frequency condition.

The flow-stress region showed stronger acoustic softening. All 15 vibration-assisted cases reduced the mean shear flow stress relative to the baseline. The reductions ranged from 30.17% to 64.52%. The flow-stress response showed a stronger dependence on amplitude, with the highest-amplitude cases generally producing the greatest reductions

Figure 11. Shear flow stress response of the baseline and vibration-assisted Fe–Ni–Cr alloy cases.

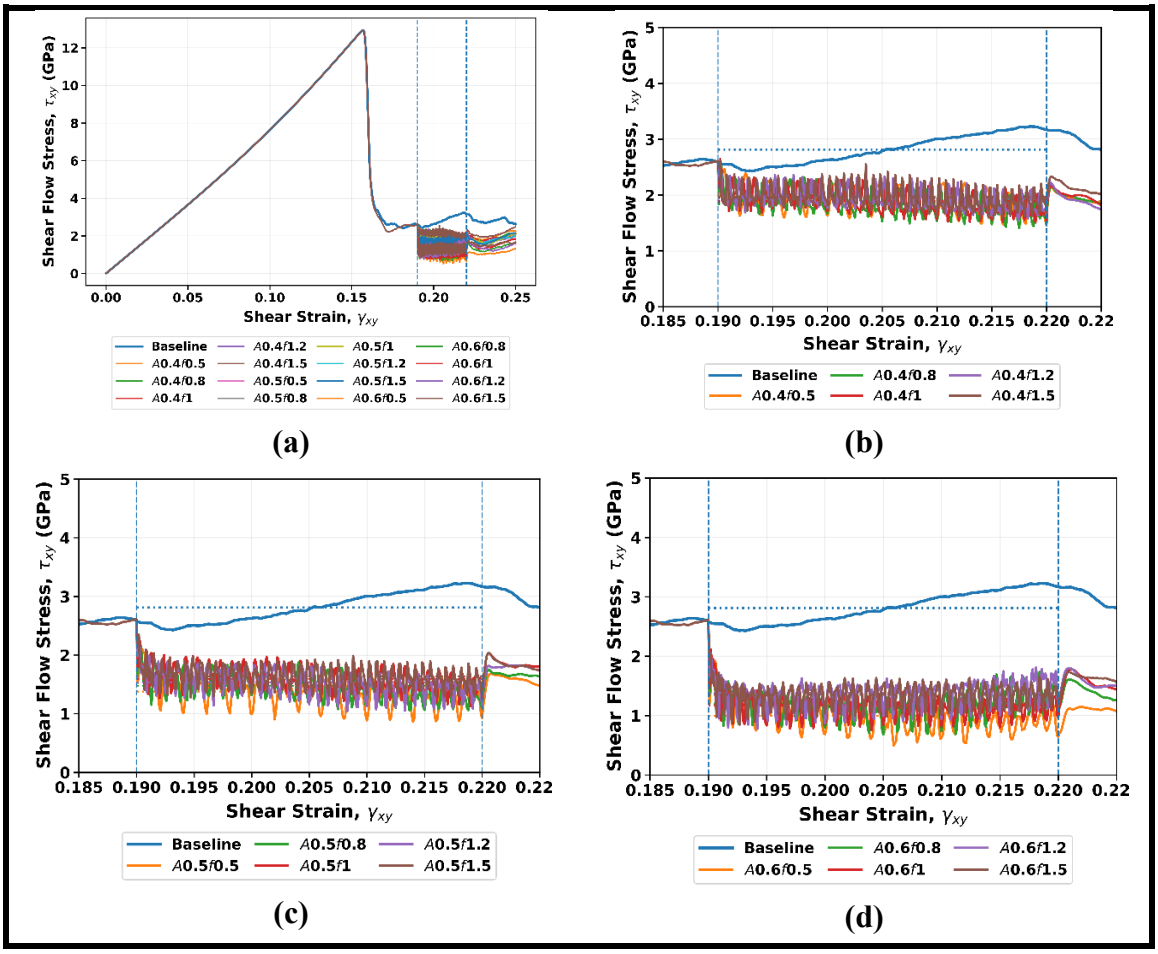

The flow-stress results are particularly relevant to AFSD because sustained material flow occurs after the onset of plastic deformation. The lower mean shear stress suggests that vibration can reduce the resistance required to maintain shear deformation. However, these results represent controlled atomistic behavior rather than direct process-scale predictions.

Defect and Dislocation Results

The defect analysis supported the stress-reduction findings. In the elastic region, the baseline alloy remained free of extracted dislocation lines through the analyzed strain range. In the vibration-assisted case, defected regions developed during vibration, and early dislocation formation was detected afterward.

In the flow-stress region, both the baseline and vibration-assisted cases began with the same dislocation structure. During vibration, the representative vibration-assisted case showed a much larger reduction in dislocation count and total dislocation line length than

the baseline. After vibration was removed and shear continued, the dislocation network formed again.

This temporary reduction suggests that vibration assisted dislocation motion, rearrangement, and annihilation. The findings indicate that the observed acoustic softening was associated with changes in the defect structure and was not caused only by stress oscillation.

Figure 12. OVITO-DXA comparison of the baseline and vibration-assisted cases in the shear flow-stress region

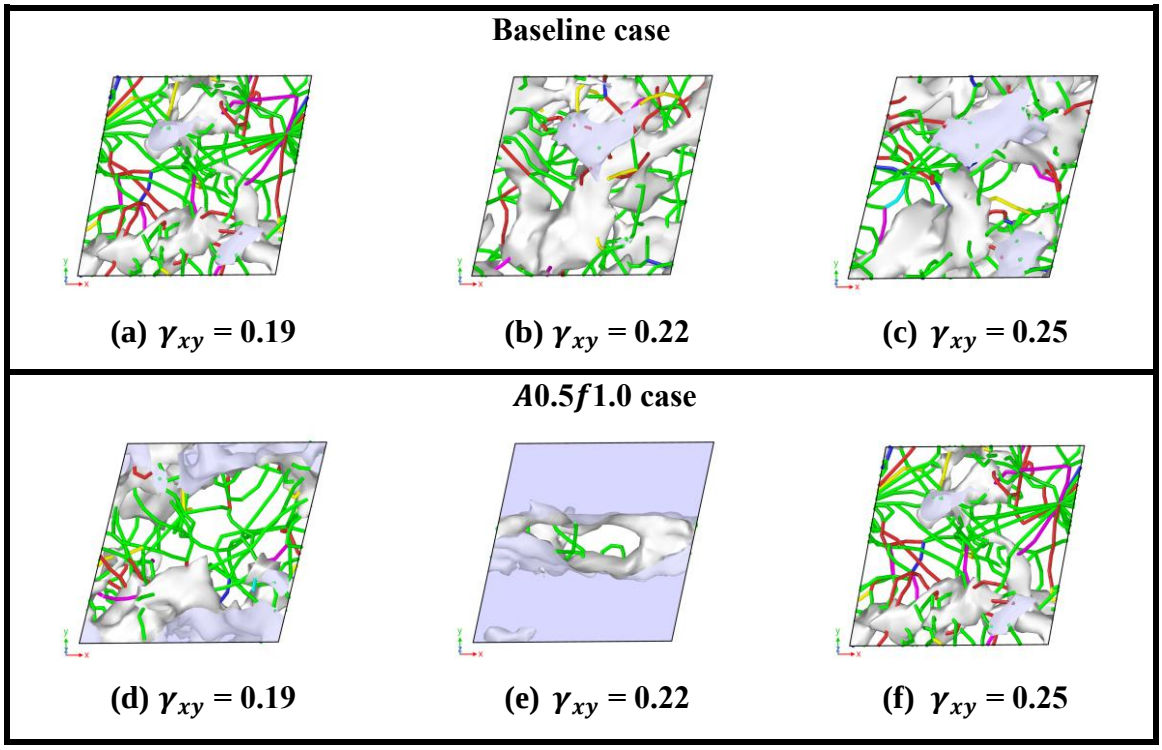

CEL Finite Element Results

The CEL model predicted temperature, equivalent stress, and material flow during stainless-steel AFSD. The mesh-convergence study showed peak temperatures of 1467°C, 1406°C, and 1403°C for the three mesh levels. The small difference between the two finer meshes indicated that the peak-temperature prediction was approaching mesh independence.

The CEL model was validated using published experimental peak-temperature data for AFSD of SS316. The validation condition included a tool rotational speed of 800 rpm, a traverse speed of 4.23 mm/s, and a material deposition rate of 0.42 mm/s. As presented in Table 3, the published experimental peak temperature was 1348.46 K, while the CEL

model predicted 1377 K. The resulting error was 2.12%, indicating good agreement between the computational prediction and the experimental result under the selected processing condition.

Table 4. Validation of the CEL Model Using Published Experimental Results

Processing parameters	Experimental result (K)	CEL model result (K)	Error (%)
Tool rotational speed: 800 rpm; traverse speed: 4.23 mm/s; material deposition rate: 0.42 mm/s	1348.46 [8]	1377	2.12

The Johnson–Cook sensitivity analysis showed that material-model selection strongly affected the FE predictions. Under fixed process conditions, the predicted peak temperature ranged from 1426°C to 1885°C, while equivalent stress ranged from 0.787 GPa to 1.876 GPa. These differences demonstrate the importance of selecting and calibrating appropriate material parameters.

Figure 13. Temperature and equivalent-stress differences obtained using two Johnson–Cook parameter sets

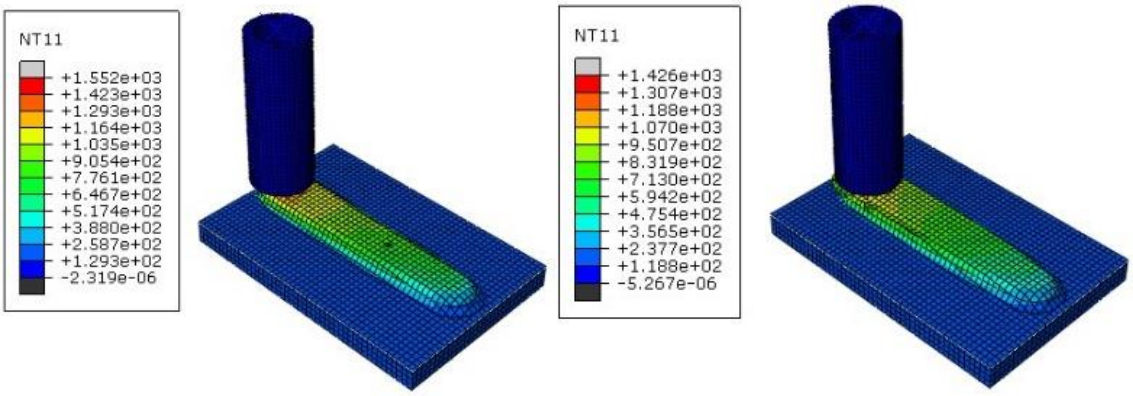

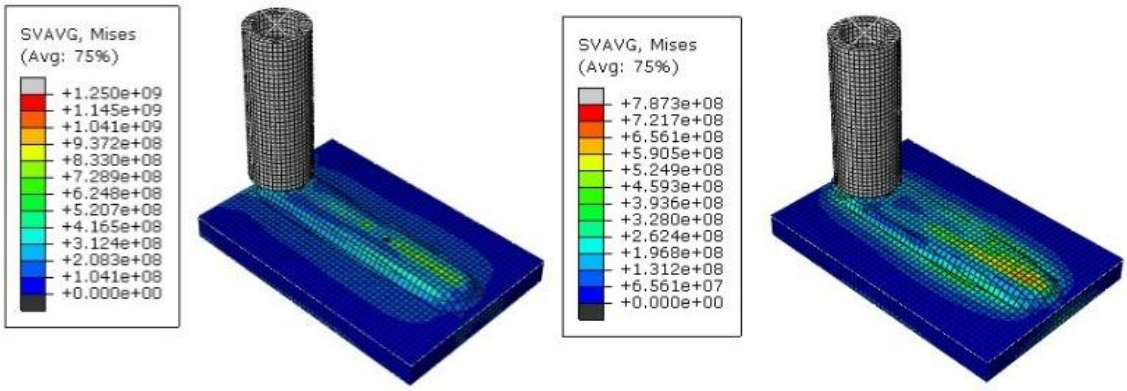

The model also reproduced different material-flow conditions. Excessive material input caused material accumulation and overflow, while low material input or high traverse speed could produce insufficient deposition. A representative balanced deposition condition was identified at 600 rpm rotational speed, 1.5 mm/s traverse speed, and 0.65 mm/s material deposition rate. This condition is specific to the current model and should be further evaluated through experiments.

Table 5. Summary of the Main Computational Findings

Study component	Main finding
Tensile MD baseline	Apparent modulus of approximately 182 GPa and maximum stress of approximately 19.5 GPa
Tensile vibration study	Apparent modulus and maximum stress changed nonlinearly with vibration amplitude and frequency
Tensile energy analysis	Kinetic energy and internal pressure generally increased with vibration, but the relationship was nonlinear
Elastic shear study	Mean shear-stress reduction of 16.41%–37.23%
Flow-stress shear study	Mean shear-stress reduction of 30.17%–64.52%
Dislocation analysis	Vibration changed defect initiation and temporarily reduced dislocation count and line length during shear flow
FE mesh analysis	Peak-temperature response approached mesh independence with refinement

FE thermal validation	2.12% error relative to published experimental peak temperature
FE material sensitivity	Johnson–Cook parameters strongly affected predicted temperature and equivalent stress
FE material flow	Model distinguished insufficient, excessive, and balanced deposition conditions

PIML Results

Numerical Digital Twin

The numerical digital twin showed strong agreement between predicted and measured melt-pool geometry. Using the interaction-based CVAE, the model achieved an overall R^2 of 0.955, with R^2 = 0.961 for width and R^2 = 0.950 for depth. The predicted values followed the measured trend closely, indicating that the model captured the nonlinear relationship between process parameters and melt-pool geometry.

The model also followed expected LPBF behavior. Increasing laser power generally increased melt-pool size, while increasing scanning speed reduced melt-pool dimensions because of lower local interaction time. This indicates that the learned mapping was not only statistically accurate but also physically consistent.

Figure 14. Predicted versus true melt-pool geometry using the numerical CVAE model [17].

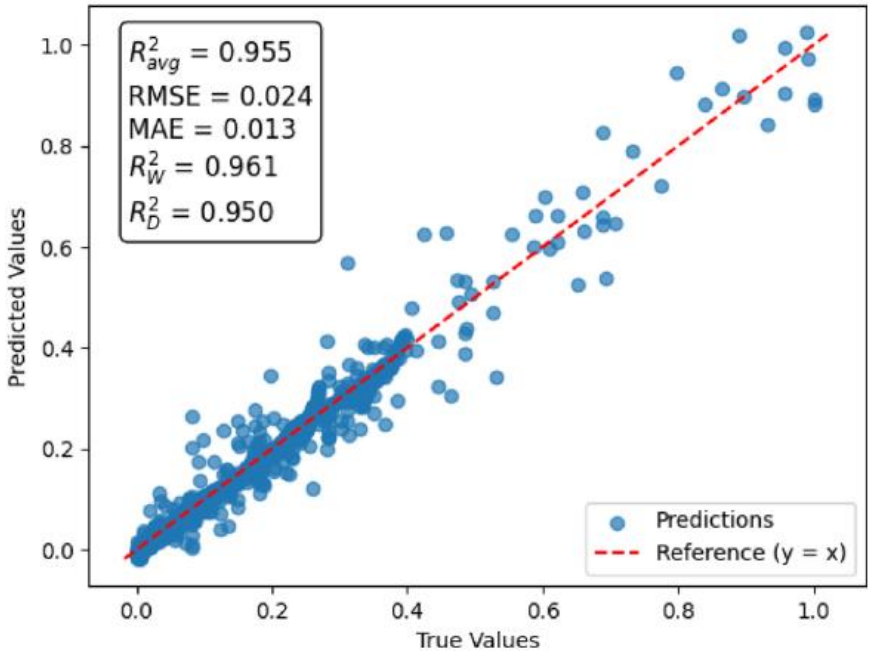

Model Performance Comparison

Table 5 compares the proposed interaction-based CNN-CVAE with classical regression and neural-network baselines under an 80/20 train-test split. The proposed model achieved the best average R^2 and the lowest MAE, showing the advantage of explicitly learning interaction-based process-geometry relationships.

Table 6. Comparison of predictive performance across different models for melt-pool width and depth under an 80/20 train-test split [17].

Model	**R^2 (Width)**	**R^2 (Depth)**	**R^2 (Avg)**	**RMSE (Avg)**	**MAE (Avg)**
Linear Regression	0.5902	0.5304	0.5603	0.0910	0.0464
Polynomial Regression	0.5753	0.5631	0.5692	0.0903	0.0433
KNN	0.7684	0.7084	0.7384	0.0699	0.0211
Random Forest Regression	0.8183	0.6193	0.7188	0.0705	0.0196
Bagging Regressor	0.8119	0.5898	0.7009	0.0726	0.0201
ANN (Independent)	0.7318	0.8246	0.7782	0.0652	0.0248
ANN (Dependent)	0.7472	0.7522	0.7497	0.0689	0.0247
Concatenation-based CNN-CVAE	0.849	0.856	0.852	0.048	0.022
CNN-CVAE (Proposed, Interaction-based)	0.864	0.875	0.870	0.046	0.017

Feature Analysis

Feature analysis was performed to evaluate the contribution of different process-parameter combinations to melt-pool geometry prediction. The best performance was obtained when all five variables were included: laser power, scanning speed, layer thickness, spot size, and porosity. This feature set achieved an overall R^2 of 0.9508, with $R^2 = 0.9564$ for width and $R^2 = 0.9452$ for depth. The result shows that even parameters with weak pairwise correlation can improve prediction when they interact with other process variables in a nonlinear way.

Table 7. Feature-combination analysis for numerical digital-twin prediction using the CVAE model.

No.	Feature Combination	Overall R^2	Width R^2	Depth R^2
1	Laser Power, Scanning Speed, Layer Thickness, Spot Size, Porosity	0.9508	0.9564	0.9452
2	Laser Power, Scanning Speed, Layer Thickness, Spot Size	0.9479	0.9492	0.9467
3	Laser Power, Scanning Speed, Layer Thickness, Porosity	0.9392	0.9515	0.9269
4	Laser Power, Scanning Speed, Layer Thickness	0.9031	0.9114	0.8949
5	Laser Power, Scanning Speed, Spot Size, Porosity	0.8831	0.9394	0.8267
6	Laser Power, Scanning Speed, Spot Size	0.8690	0.9157	0.8223
7	Laser Power, Scanning Speed, Porosity	0.8595	0.9159	0.8031
8	Laser Power, Scanning Speed	0.8260	0.8836	0.7684

Image-Based and Hybrid Digital Twin

The image-based model demonstrated the feasibility of reconstructing melt-pool cross-sectional images from limited image data. The single-stage image-based CVAE achieved an image reconstruction R^2 of 0.7691. The hybrid two-stage model, which first predicted geometry and then used the geometry-conditioned image model, improved the reconstruction performance to $R^2 = 0.7790$. Because only 23 calibrated images were available, these results should be interpreted as a proof-of-concept for image-based digital-twin development.

Figure 15. Original melt-pool images and corresponding reconstructions generated by Stage 2 of the hybrid digital twin [17].

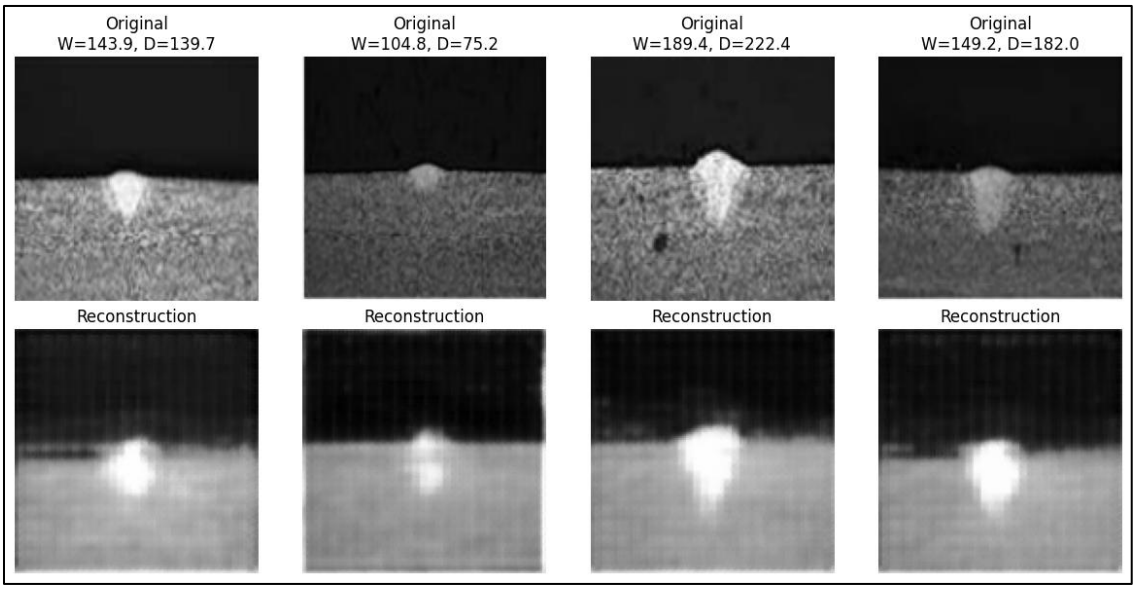

Figure 16. Illustrative example of the hybrid digital twin operating as a generative model [17].

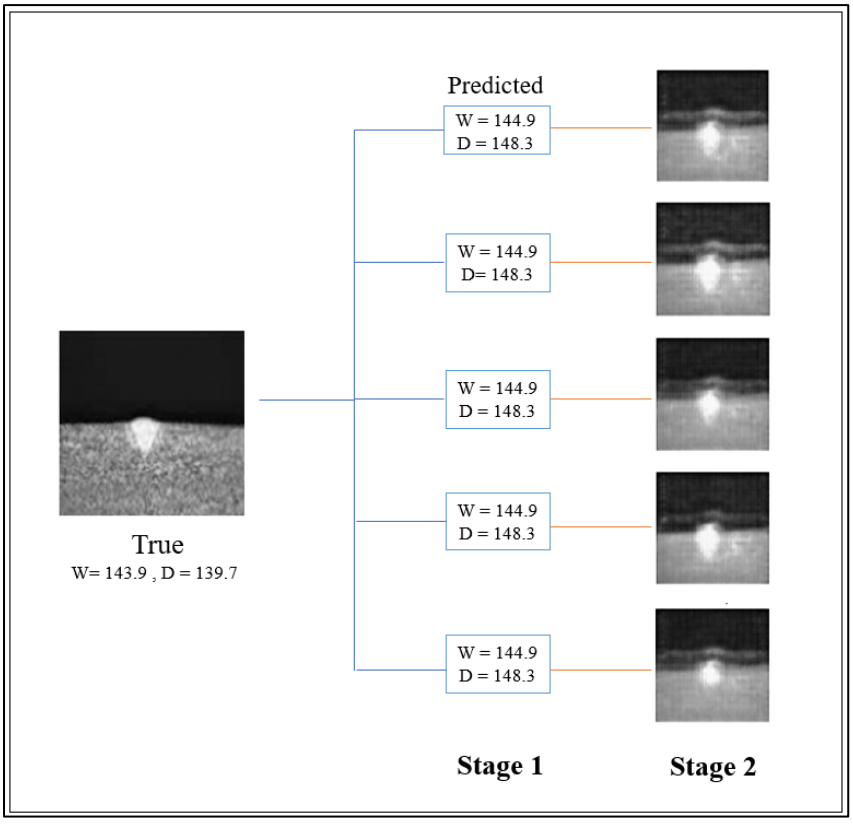

Reverse Digital Twin

The reverse digital twin inferred feasible process-parameter combinations from a target melt-pool width and depth. The reverse CVAE achieved $R^2 = 0.634$, which indicates moderate but physically meaningful performance for an inverse problem. This lower value is expected because the reverse LPBF mapping is ill-posed and non-unique. Unlike forward prediction, where a given process-parameter set produces a specific melt-pool response, the same melt-pool geometry can be produced by several different combinations of laser power, scanning speed, layer thickness, spot size, and porosity.

Therefore, the reverse model was evaluated as a distribution-learning framework rather than as a single deterministic predictor. As shown in Figure 17, the median predictions follow the overall ground-truth trend, while the spread within each bin reflects the existence of multiple physically feasible parameter combinations. This prediction spread is not only model error; it also represents the natural ambiguity of inverse process design.

The coefficient of variation was used to interpret prediction differences relative to the natural variability of each melt-pool regime. Parameters with limited variation, such as spot size and porosity, require tighter prediction accuracy because small absolute deviations become statistically significant. In contrast, regimes with larger dispersion allow a wider range of physically plausible inverse solutions. Therefore, the reverse-model result should be interpreted in the context of data sparsity, limited parameter-space coverage, and the inherent non-uniqueness of the inverse LPBF problem.

Figure 17. Box-plot visualization of reverse-model predictions grouped by true scaled process-parameter bins [17].

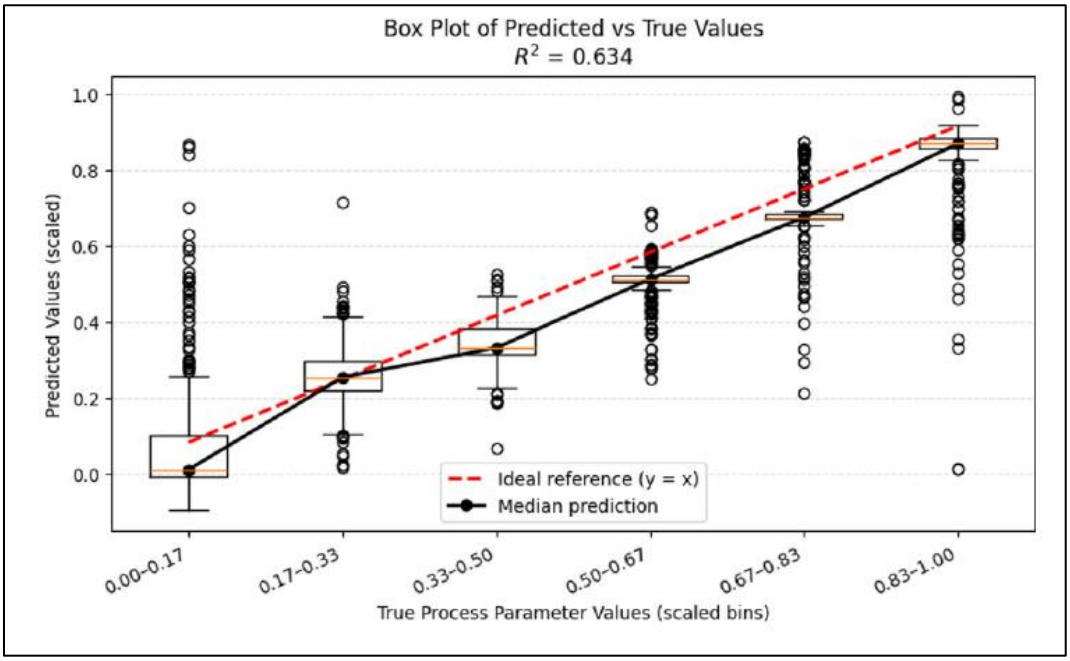

Overall, the results show that the proposed physics-inspired CVAE framework can support both forward melt-pool prediction and reverse process-parameter inference under limited-data conditions. The interaction-based architecture improved predictive performance compared with conventional baselines, while the hybrid and reverse models extended the framework toward image reconstruction and inverse process design.

PIML Model Limitations and Future Work

Although the LPBF-based PIML framework demonstrated strong forward-prediction capability, several limitations should be considered when interpreting the results. The numerical dataset was compiled from multiple sources, and compatibility-based filtering was applied to retain data collected under comparable LPBF conditions, similar powder characteristics, and standardized measurement procedures. However, residual inter-source variability may still influence model performance. The image-based model was also constrained by the availability of only 23 calibrated melt-pool cross-sectional images, which limits statistical generalization. Therefore, the image-based and hybrid components should be interpreted as proof-of-concept digital-twin models rather than fully validated production-level tools. In addition, the reverse model was affected by the inherent non-uniqueness of inverse LPBF design, where multiple combinations of laser power, scanning speed, layer thickness, spot size, and porosity may produce similar melt-pool geometries. This limitation is more pronounced in sparsely represented melt-pool regimes.

Future work should expand the LPBF dataset through controlled experiments, include more calibrated cross-sectional images, and validate the framework using unseen builds and broader processing conditions. Integrating in-process measurement data or sensor feedback, along with stronger physics-based constraints, could improve model robustness, reduce physically inconsistent predictions, and strengthen reverse-design capability.

Building on this direction, we extended the small-dataset machine-learning approach to Wire-Arc Additive Manufacturing (WAAM), where limited experimental data and process variability also present major challenges for parameter selection. In our related study, machine learning was used to analyze process-parameter effects in wire-arc additively manufactured 316 stainless steel using a small dataset. This work was accepted for publication in the *Proceedings of the American Society of Mechanical Engineers (ASME) 2026 International Mechanical Engineering Congress and Exposition (IMECE*

2026) [22]. The accepted WAAM study broadens the impact of the present work by demonstrating that data-efficient machine-learning strategies can be transferred from powder-bed fusion to wire-arc deposition systems. Together, these studies establish a broader pathway toward small-dataset-driven parameter analysis, process understanding, and future qualification of data-limited metal additive manufacturing processes.

Conclusions

This project established a computational framework for studying the thermomechanical response of stainless steel during Additive Friction Stir Deposition. The project combines molecular dynamics, CEL finite element modeling, physics-informed machine learning, and experimental validation.

The tensile MD simulations showed that ultrasonic vibration changed the apparent stiffness, maximum stress, kinetic energy, and internal pressure of the Fe–Ni–Cr alloy. The response depended on both vibration amplitude and frequency and was not consistently linear.

The shear MD simulations showed that vibration reduced mean shear stress in both the elastic and flow-stress regions. The flow-stress region produced greater reductions and showed a clearer dependence on vibration amplitude. Defect analysis indicated that vibration modified dislocation formation, motion, rearrangement, and annihilation.

The CEL model successfully represented temperature, stress, material flow, and deposition behavior during stainless-steel AFSD. The model showed good agreement with published peak-temperature data and was able to distinguish between excessive and balanced deposition conditions.

The FE results also showed that constitutive-material parameters strongly influence predicted temperature and stress. This finding supports the inclusion of atomic-scale analysis, experimental calibration, and physics-informed machine learning in the broader framework.

The physics-informed machine learning component was completed using a different material system than originally proposed. Stainless steel AFSD does not yet have a process-response dataset large or consistent enough to train and validate a predictive model, and the supporting experiments were not completed within the project period. The methodology was therefore developed and validated using laser powder bed fusion data for Ti–6Al–4V. The interaction-based conditional variational autoencoder achieved an overall R^2 of 0.955 on the full dataset and 0.870 under an 80/20 train-test split for forward geometry prediction, and it outperformed conventional regression and neural-network baselines. The same framework also performed inverse estimation of process parameters from a target geometry. Because the architecture takes process parameters as

inputs and geometric response as output, without assuming a melting-based mechanism, it can be retrained on AFSD data without structural modification. This component is therefore a validated and transferable methodology rather than a stainless-steel predictive model, and it represents the machine learning capability that the broader framework requires.

The present MD and FE models provide mechanism-level and process-level information, respectively. Further integration and experimental validation are needed before the framework can be used for direct process optimization or infrastructure implementation.

Recommendations

The project tasks have been successfully completed but the PI has faced some challenges regarding experimental data availability and modeling complications. Based on the overall experience, recommendations and future work are listed below:

1. The Johnson–Cook parameters should be calibrated using temperature-dependent stainless-steel data covering AFSD-relevant temperature, strain, and strain-rate conditions.

2. CEL model validation should be expanded beyond a single peak-temperature comparison. Future validation should include temperature history, deposited-layer geometry, tool force, torque, and material-flow behavior.

3. Experiments using the MELD L3 equipment should be conducted under multiple rotational speeds, traverse speeds, and material deposition rates.

4. The CEL model should be extended to include multilayer deposition, improved tool heat transfer, and more detailed contact behavior.

5. The physics-informed machine learning model should combine physical constraints with MD, FE, and experimental data from AFSD of 316 stainless steel.

6. The MD simulations should be extended to investigate alloy composition, temperature, strain rate, system size, and initial defect conditions.

7. Additional dislocation analysis should be conducted for all major vibration conditions rather than only representative cases.

8. Direct transfer of MD stress values into the FE model should be avoided until a suitable scale-bridging approach is developed.

9. Process parameters should be optimized together because rotational speed, traverse speed, and deposition rate interact strongly.

10. Future implementation studies should focus on specific infrastructure applications such as bridge repair, rail-component restoration, pipeline reinforcement, and remanufacturing of transportation components.

Acronyms, Abbreviations, and Symbols

Term	Description
AFSD	Additive Friction Stir Deposition
AM	Additive Manufacturing
CEL	Coupled Eulerian–Lagrangian
DXA	Dislocation Extraction Algorithm
FE	Finite Element
FCC	Face-Centered Cubic
FSP	Friction Stir Processing
FSW	Friction Stir Welding
LAMMPS	Large-scale Atomic/Molecular Massively Parallel Simulator
LTRC	Louisiana Transportation Research Center
MD	Molecular Dynamics
MEAM	Modified Embedded Atom Method
NPT	Constant number of atoms, pressure, and temperature ensemble
NVT	Constant number of atoms, volume, and temperature ensemble
OVITO	Open Visualization Tool
PIML	Physics-Informed Machine Learning
SS316	Type 316 Stainless Steel
SS316L	Low-carbon Type 316 Stainless Steel
USV	Ultrasonic Vibration
A	Vibration amplitude or Johnson–Cook yield constant, depending on context
f	Vibration frequency
T	Temperature
γ_{xy}	Engineering shear strain
σ_y	Flow stress
τ	Shear stress
λ	Wavelength
ω	Angular frequency

References

[1] H. Z. Yu and R. S. Mishra, “Additive Friction Stir Deposition: A Deformation Processing Route to Metal Additive Manufacturing,” *Materials Research Letters*, vol. 9, no. 2, pp. 71–83, 2021.

[2] C. Mason, R. Rodriguez, D. Avery, B. Phillips, B. Bernarding, M. Williams, S. Cobbs, J. Jordon, and P. P. Allison, “Process Structure Property Relations for As-Deposited Solid-State Additively Manufactured High-Strength Aluminum Alloy,” *Additive Manufacturing*, vol. 40, p. 101879, 2021.

[3] C. S. Alam, V. Karami, S. Guo, and M. S. Rahman, “Thermo-Mechanical Response of Aluminum Alloy in the Additive Friction-Stir Deposition Process,” *Additive Manufacturing Letters*, vol. 12, p. 100263, 2025.

[4] American Road and Transportation Builders Association, “Louisiana Bridge Condition Report.” [Online]. Available: https://artbabridgereport.org/state/profile/LA. [Accessed: Feb. 20, 2025].

[5] Federal Railroad Administration, “Rail Base Corrosion and Cracking Prevention,” U.S. Department of Transportation. [Online]. Available: https://railroads.dot.gov/elibrary/rail-base-corrosion-and-cracking-prevention. [Accessed: Feb. 20, 2025].

[6] American Iron and Steel Institute, “AISI Releases Annual Statistical Report for 2021,” 2022. [Online]. Available: https://www.steel.org/2022/09/aisi-releases-annual-statistical-report-for-2021. [Accessed: Feb. 20, 2025].

[7] D. D’Andrea, “Additive Manufacturing of AISI 316L Stainless Steel: A Review,” *Metals*, vol. 13, no. 8, p. 1370, 2023.

[8] P. Agrawal, R. S. Haridas, S. Yadav, S. Thapliyal, A. Dhal, and R. S. Mishra, “Additive Friction Stir Deposition of SS316: Effect of Process Parameters on Microstructure Evolution,” *Materials Characterization*, vol. 195, p. 112470, 2023.

[9] M. V. Gor, M. Barnett, D. Fabijanic, and P. P. Bhattacharjee, “Additive Friction Stir Deposition of Super Duplex Stainless Steel: Microstructure and Mechanical Properties,” *Additive Manufacturing Letters*, vol. 9, p. 100204, 2024.

[10] G. G. Stubblefield, K. Fraser, B. Phillips, J. Jordon, and P. Allison, “A Meshfree Computational Framework for the Numerical Simulation of the Solid-State Additive Manufacturing Process, Additive Friction Stir-Deposition,” *Materials & Design*, vol. 202, p. 109514, 2021.

[11] F. Al-Badour, N. Merah, A. Shuaib, and A. Bazoune, “Coupled Eulerian Lagrangian Finite Element Modeling of Friction Stir Welding Processes,” *Journal of Materials Processing Technology*, vol. 213, no. 8, pp. 1433–1439, 2013.

[12] J. Peng et al., “Coupling Physics in Machine Learning to Predict Properties of High-Temperature Alloys,” *npj Computational Materials*, vol. 6, no. 1, p. 141, 2020.

[13] Y. Du, T. Mukherjee, and T. DebRoy, “Physics-Informed Machine Learning and Mechanistic Modeling of Additive Manufacturing to Reduce Defects,” *Applied Materials Today*, vol. 24, p. 101123, 2021.

[14] A. A. Kabhi, P. Nourian, and M. S. Rahman, “Effect of Ultrasonic Vibration on the Solid-State Processing of Stainless Steel: An Atomic-Scale Analysis of the Fe–Ni–Cr Ternary System,” *Proceedings of the ASME 2025 International Mechanical Engineering Congress and Exposition*, Memphis, Tennessee, USA, IMECE2025-166646, 2025.

[15] A. A. Kabhi, H. Sharifi, S. A. Shuvo, M. A. Siddiquee, and M. S. Rahman, “Atomistic Investigation of Acoustic Softening and Dislocation Behavior in the Fe–Ni–Cr Ternary System for Solid-State Manufacturing in Space,” manuscript prepared for the *ASME 2026 International Mechanical Engineering Congress and Exposition*, Vancouver, British Columbia, Canada, IMECE2026-191739, 2026.

[16] M. A. Siddiquee, A. A. Kabhi, S. A. Shuvo, P. Sarker, and M. S. Rahman, “Modeling and Parametric Analysis of Additive Friction Stir Deposition for Stainless Steel Using a Coupled Eulerian–Lagrangian Approach,” manuscript prepared for the *ASME 2026 International Mechanical Engineering Congress and Exposition*, Vancouver, British Columbia, Canada, IMECE2026-191764, 2026.

[17] S. A. Shuvo, X. Liu, and M. S. Rahman, “A Bidirectional Physics-Inspired Digital Twin for Melt-Pool-Process Parameter Interplay in Laser Powder-Bed Fusion,” Journal of Intelligent Manufacturing, 2026. https://doi.org/10.1007/s10845-026-02922-3

[18] Jiang, F., Xia, M., & Hu, Y. (2024). Physics-informed machine learning for accurate prediction of temperature and melt pool dimension in metal additive manufacturing. 3D Printing and Additive Manufacturing, 11(4), 1679–1689. https://doi.org/10.1089/3dp.2022.0363

[19] Peng, B., & Panesar, A. (2024). Multi-layer thermal simulation using physics-informed neural network. Additive Manufacturing, 95, Article 104498. https://doi.org/10.1016/j.addma.2024.104498

[20] Li, Y., Mojumder, S., Lu, Y., Al Amin, A., Guo, J., Xie, X., Chen, W., Wagner, G. J., Cao, J., & Liu, W. K. (2024). Statistical parameterized physics-based machine learning digital shadow models for laser powder bed fusion process. Additive Manufacturing, 87, Article 104214. https://doi.org/10.1016/j.addma.2024.104214

[21] Mathew, A. N., Pandurangan, V., & Venkaiah, N. (2026). Physics-informed intelligent framework for geometric prediction and compensation in metal additive manufacturing. Journal of Intelligent Manufacturing. https://doi.org/10.1007/s10845-026-02883-7

[22] Shuvo, S. A., Kabhi, A. A., Siddiquee, M. A., Liu, X., Thapliyal, S., and Rahman, M. S., 2026, “Machine Learning Assisted Process Parameter Analysis of Wire-Arc Additively Manufactured 316 Stainless Steel Using a Small Dataset,” Proceedings of the ASME 2026 International Mechanical Engineering Congress and Exposition, Vancouver, British Columbia, Canada, Nov. 8–12, 2026, Paper No. IMECE2026-191768, accepted for publication.

Appendix

Graduate Students who Got Support from This Project

1. Ahsanul Alam Kabhi (Ph.D.), Louisiana Tech University
2. Md Ashfaq Siddiquee (Ph.D.), Louisiana Tech University
3. Sabbir Alom Shuvo (Ph.D.), Louisiana Tech University

Publications List

A. Journal Publications Generated from this Project

Under Preparation:

1. Kabhi, A. A., Sharifi, H., Mahata, A., and Rahman, M. S. (2026). Molecular Dynamics Study of Acoustic Softening and Dislocation-Mediated Deformation in Fe–Ni–Cr Alloys under Ultrasonic Vibration-Assisted Shear. Mechanics of Materials, manuscript under preparation.
2. Rahman, M.S., Hofmann, D., Nourian, P., Kabhi, A. A., Siddiquee, M. A., Hossain, R., Sharifi, H., Kekeli, Yasmin, M., Alam, C.S., Lee, H., Zeng, C. S., Shuvo, S.A., Murray, E., Weiss, L., Sarker, P., and Moore, A. L. (2026). Additive Friction Stir Deposition for Aerospace Applications: Technology Maturity, Challenges, and Pathways to Deployment. Materials and Manufacturing Processes, manuscript under preparation.

Already Published:

1. Shuvo, S. A., Liu, X., and Rahman, M. S. (2026). A Bidirectional Physics-Inspired Digital Twin for Melt-Pool-Process Parameter Interplay in Laser Powder Bed Fusion. Journal of Intelligent Manufacturing. https://doi.org/10.1007/s10845-026-02922-3
2. Hassan, S., Shuvo, S. A., Alam, J. U., Islam, N., Islam, M. F. A., Rahman, Y., Nabi, I., Yeasmin, F., Siddiquee, M. A., Kabhi, A. A., Hosain, M., and Rahman, M. S. (2026). Thin-Film Solar Cells for Solar Thermal Cooling, Heating, and

Energy Storage Systems: Materials, Manufacturing, and Emerging Applications. Energies, 19(11), 2684. https://doi.org/10.3390/en19112684

B. Peer-Reviewed Conference Papers (All are accepted in ASME IMECE 2026, the largest international conference in Mechanical Engineering)

1. Kabhi, A. A., Sharifi, H., Shuvo, S. A., Siddiquee, M. A., and Rahman, M. S., 2026, "Atomistic Investigation of Acoustic Softening and Dislocation Behavior in the Fe–Ni–Cr Ternary System for Solid-State Manufacturing in Space," Proceedings of the ASME 2026 International Mechanical Engineering Congress and Exposition, Vancouver, British Columbia, Canada, Nov. 8–12, 2026, Paper No. IMECE2026-191739, accepted for publication.

2. Siddiquee, M. A., Kabhi, A. A., Shuvo, S. A., Alam, C. S., and Rahman, M. S., 2026, "Additive Friction Stir Deposition of Lunar Regolith Integrated Aluminum Alloy for Space Manufacturing and Repair," Proceedings of the ASME 2026 International Mechanical Engineering Congress and Exposition, Vancouver, British Columbia, Canada, Nov. 8–12, 2026, Paper No. IMECE2026-193371, accepted for publication.

3. Siddiquee, M. A., Kabhi, A. A., Shuvo, S. A., Sarker, P., and Rahman, M. S., 2026, "Modeling and Parametric Analysis of Additive Friction Stir Deposition for Stainless Steel Using a Coupled Eulerian–Lagrangian Approach," Proceedings of the ASME 2026 International Mechanical Engineering Congress and Exposition, Vancouver, British Columbia, Canada, Nov. 8–12, 2026, Paper No. IMECE2026-191764, accepted for publication.

4. Shuvo, S. A., Kabhi, A. A., Siddiquee, M. A., Liu, X., Thapliyal, S., and Rahman, M. S., 2026, "Machine Learning Assisted Process Parameter Analysis of Wire-Arc Additively Manufactured 316 Stainless Steel Using a Small Dataset," Proceedings of the ASME 2026 International Mechanical Engineering Congress and Exposition, Vancouver, British Columbia, Canada, Nov. 8–12, 2026, Paper No. IMECE2026-191768, accepted for publication.